PHYSICAL REVIEW D **91,** 083001 (2015)

# Astrophysics of resonant orbits in the Kerr metric

Jeandrew Brink,[1,2] Marisa Geyer,[3,4] and Tanja Hinderer[5]

[1]*National Institute for Theoretical Physics (NITheP), Bag X1 Matieland, Stellenbosch 7602, South Africa*
[2]*Department of Applied Mathematics, Stellenbosch University, Stellenbosch 7602, South Africa*
[3]*Physics Department, Stellenbosch University, Stellenbosch 7602, South Africa*
[4]*Department of Astrophysics, University of Oxford, Oxford OX1 3RH, United Kingdom*
[5]*Department of Physics, Maryland Center for Fundamental Physics & Joint Space-Science Institute, University of Maryland, College Park, Maryland 20742, USA*

(Received 5 February 2015; published 2 April 2015)

This paper gives a complete characterization of the location of resonant orbits in a Kerr spacetime for all possible black hole spins and orbital parameter values. A resonant orbit in this work is defined as a geodesic for which the longitudinal and radial orbital frequencies are commensurate. Our analysis is based on expressing the resonance condition in its most symmetric form using Carlson's elliptic integrals, which enable us to provide exact results together with a number of concise formulas characterizing the explicit dependence on the system parameters. The locations of resonant orbits identify regions where intriguing observable phenomena could occur in astrophysical situations when various sources of perturbation act on the binary system. Resonant effects may have observable implications for the inspirals of compact objects into a supermassive black hole. During a generic inspiral the slowly evolving orbital frequencies will pass through a series of low-order resonances where the ratio of orbital frequencies is equal to the ratio of two small integers. At these locations rapid changes in the orbital parameters could produce a measurable phase shift in the emitted gravitational and electromagnetic radiation. Resonant orbits may also capture gas or larger objects leading to further observable characteristic electromagnetic emission. According to the Kolmogorov-Arnold-Moser theorem, low-order resonant orbits demarcate the regions where the onset of geodesic chaos could occur when the Kerr Hamiltonian is perturbed. Perturbations are induced for example if the spacetime of the central object is non-Kerr, if gravity is modified, if the orbiting particle has large multipole moments, or if additional masses are nearby. We find that the $1/2$ and $2/3$ resonances occur at approximately 4 and 5.4 Schwarzschild radii ($R_s$) from the black hole's event horizon. For compact object inspirals into supermassive black holes ($\sim 10^6 M_\odot$) this region lies within the sensitivity band of space-based gravitational wave detectors such as eLISA. When interpreted within the context of the supermassive black hole at the Galactic center, Sgr A*, this implies that characteristic length scales of 41 $\mu$as and 55 $\mu$as and time scales of 50 min and 79 min respectively should be associated with resonant effects if Sgr A* is nonspinning, while spin decreases these values by up to $\sim$32% and $\sim$28%. These length scales are potentially resolvable with radio very-long-baseline interferometry measurements using the Event Horizon Telescope. We find that all low-order resonances are localized to the strong field region. In particular, for distances $r > 50R_s$ from the black hole, the order of the resonances is sufficiently large that resonant effects of generic perturbations are not expected to lead to drastic changes in the dynamics. This fact guarantees the validity of using approximations based on averaging to model the orbital trajectory and frequency evolution of a test object in this region. Observing orbital motion in the intermediate region $50R_s < r < 1000R_s$ is thus a "sweet spot" for systematically extracting the multipole moments of the central object by observing the orbit of a pulsar—since the object is close enough to be sensitive to the quadruple moment of the central object but far enough away not to be subjected to resonant effects.

DOI: 10.1103/PhysRevD.91.083001 PACS numbers: 98.35.Jk, 04.20.Dw, 97.60.Lf, 98.62.Js

## I. INTRODUCTION

Supermassive black holes such as Sgr A* at the center of our Galaxy are at zeroth order mathematically idealized as Kerr black holes. In practice this description is not complete due to a plethora of small perturbing effects which slightly alter the spacetime geometry. In general these perturbations are small and well accounted for with canonical perturbation theory. In the special case that the perturbation excites one of the intrinsic resonant structures of the spacetime's orbits, the effect may be larger than expected due to an anomalous transfer of energy and angular momentum that occurs during such a perturbation. Resonance phenomena are ubiquitous in any multifrequency system. In celestial mechanics they strongly influence satellite dynamics and ring formation. Examples include the gaps in the asteroid belt between Mars and Jupiter [1] and the gaps in the rings of Saturn [2–4]. Resonances are further intimately connected with the onset of dynamical chaos [5].

 

As radio telescopes increase in sensitivity and collecting area they will be able to resolve length scales typical of resonant phenomena in the spacetime of the black hole at the center of our Galaxy. The Event Horizon Telescope is one such observational tool currently under development [6]. Space-based gravitational wave detectors such as eLISA may observe shifts in the phasing of the gravitational waves emitted during the inspiral of a compact object as it passes through the various resonant bands. X-ray, optical and infrared telescopes do not have the resolving power to image Sgr A* directly, but can potentially record flux variations from this region that may display time scales characteristic of resonant events.

This paper investigates resonant orbits in the Kerr metric expanding on the discussion in [7]. The aim is to provide a complete characterization of the parameter space where resonant orbits occur as a function of black hole spin and the orbital parameters. Since geodesic orbital motion in Kerr is completely integrable, it is akin to geodesic flow on a two-dimensional torus in phase space. Generic orbits are ergodic and sample the entire surface of the torus after a sufficiently long time. Low-order resonant orbits however only trace out a simple, codimension-one curve on the torus. Some of the features of resonant orbital trajectories are illustrated in [8–12]. By the Kolmogorov-Arnold-Moser (KAM) theorem which is discussed in Sec. II, low-order resonant orbits are most likely to exhibit the nonsmooth anomalous behavior associated with a rapid change in the constants of motion and the breaking of the resonant torus. Test particles entering a low-order resonance often display subsequent dynamics with a sensitive dependence on initial conditions.

To date a number of authors have studied resonant effects in Kerr-like metrics in the context of various forms of perturbations. The effect of perturbations originating from adding a quadruple moment to the Kerr metric has been quantified by exploring orbital motion in the Manko-Novikov metric [13–17]. Perturbations from the presence of a disk were considered in Ref. [18], and the effects of the small mass's spin in [19–21]. The features of traversing a resonance during an inspiral, where the perturbation arises from the small mass's gravitational self-force, have been explored by [22,23], and the possibility of sustained resonance has been considered in [24]. Resonances involving one of the fundamental frequencies of the motion on the torus and the orbit's rotational frequency were studied in the context of enhanced gravitational recoil [25,26], and isofrequency orbits were discussed in [27].

Most of these studies have focused on a particular orbital trajectory or a small subset of parameters in a specific perturbed setting. The idea of this paper is to refrain from specializing to a particular perturbation and instead provide insights that apply to all types of resonant behavior. We will use tools such as the results of the KAM theorem that hold true regardless of the source of perturbation. The results obtained here are thus robust in the sense that the time and length scales of resonance effects for astrophysical applications are to be associated with properties of the underlying Kerr metric and resonance location rather than the details of the effect causing the perturbation. The aim of this paper is to make the typical resonance time and length scales accessible to the larger astrophysics community by means of easily evaluated formulas and tabulated results.

To explore the resonance effects we describe the orbits in the Kerr metric using a set of variables adapted to the orbital geometry [28] that reduce to the Keplerian orbital parameters in the Newtonian limit rather than the constants of motion associated with the spacetime's Killing fields. The properties of the Keplerian constants will be reviewed in Sec. III A. Plotting the location of resonances in terms of these variables immediately allows us to interpret the result as a physical location in the actual spacetime.

The resonances considered in this paper arise due to the libration frequencies associated with the longitudinal and radial motion around the black hole discussed further in Sec. III A. These two frequencies are particularly important for the systematic study of the breakup of resonant tori in systems where the azimuthal Killing vector is maintained. In this case the $\phi$-motion and associated frequency, $\omega_\phi$, is computed once the librational motions have been determined and plays a passive role in the dynamics. The two libration frequencies further play a dominant role in the computed gravitational wave phase shift during resonant passage in an extreme mass ratio inspiral. The $\omega_\phi$ frequency only contributes to the phase shift at higher order in mass ratio [29]. In the context of the resonances observed in quasiperiodic oscillations (QPOs), Török *et al.* [30] argue that it is more difficult to find a plausible explanation involving the $\omega_\phi$ frequency than a mechanism involving the libration frequencies, although such possibilities do exist. Discussions of resonant effects associated with the $\omega_\phi$ frequency can be found in [12,26,31].

A resonant orbit in this work occurs if the ratio of the characteristic radial, $\omega_r$, and longitudinal, $\omega_\theta$, frequencies is a rational fraction, $\omega_r/\omega_\theta = n/m$ where $n, m \in \mathbb{N}$. Most of the technical aspects of this paper deal with how to efficiently examine this expression and extract the physics. Closed-form analytic expressions for the frequencies in terms of elliptic integrals have been presented by [28,32] which serve as companions to this work. Here, however, we opt in Sec. IV to take advantage of a more symmetric representation of the elliptic functions appearing in the resonance condition and write them in terms of Carlson's integrals [33–35]. This allows us to identify the important parameters in the problem and exploit the identities associated with Carlson's integrals to manipulate the expressions. In Sec. V we consider solutions to the resonance condition. We first specialize to the weak field limit where we introduce the key properties of a "resonant surface" in the parameter space. We then give a number of

exact analytic solutions to the resonance condition that can be used to describe resonances in the strong field region near the black hole. Finally, several low-order (small $n+m$ value) resonant surfaces such as the $1/2$, $2/3$ and $3/4$ are evaluated numerically and compared to the analytic results and approximate formulas.

The breakdown of integrability around a resonance in "almost"-Kerr spacetimes is often quantified by numerically generating Poincaré maps for a fixed energy $E$ and angular momentum component $L_z$. Associated with each Poincaré plot is a rotation curve which characterizes the frequency ratio as a function of initial condition given a fixed $E$ and $L_z$. In Sec. VII we give a representative example of orbital breakdown around the $2/3$ resonance and analytically compute Kerr's rotation curve. We further provide expressions for finding the $E$ and $L_z$ values associated with a particular resonance.

The exact nature of a perturbed system's response in the region of a resonance depends on the source of perturbation. In Sec. VIII we heuristically discuss how one would estimate the size of a perturbation required to see a dramatic change in dynamics. It is important to note that the KAM theorem does not guarantee the breakdown of integrability at any particular resonance. It merely states that if integrability breaks down it will occur first at the location of a low-order resonant orbit.[1] Since this is true of all possible sources of perturbation, the cumulative effect of many sources of perturbation could result in a Saturn ringlike structure (see Fig. 16) being established around the black hole. This and other potentially observable effects due to resonances are discussed in Sec. IX. We focus in particular on the Galactic center, Sgr A*, as a possible observational realization of an extreme mass ratio inspiral (EMRI). We note which detectors will be sensitive to resonant orbits as well as the implications of regions where we can guarantee the absence of low-order resonances and in which we expect orbits to be approximately integrable. Regions that only contain high-order resonances we consider to be the "sweet spot" for observationally determining the higher-order multipole moments of the supermassive black hole in the Milky way.

## II. KAM THEOREM AND IMPORTANCE OF RESONANT ORBITS

Bound geodesic motion in the Kerr spacetimes is integrable [36] since the Hamiltonian $\mathcal{H}_K = 1/2 g_K^{\mu\nu} p_\mu p_\nu$, where $g_K^{\mu\nu}$ is the inverse Kerr metric and $p_\mu$ the test particle's four-momentum, admits a full set of isolating integrals. Two of these integrals result from the absence of explicit time and azimuthal dependence in the Kerr metric functions, the third is due to the conservation of rest mass and the fourth integral is known as the Carter constant [36]. Integrability implies that action-angle variables can be defined. The phase space is foliated by invariant level surfaces of the actions with the compact dimensions of these surfaces diffeomorphic to a torus. Geodesic motion in an integrable system is thus akin to geodesic flow on a torus.

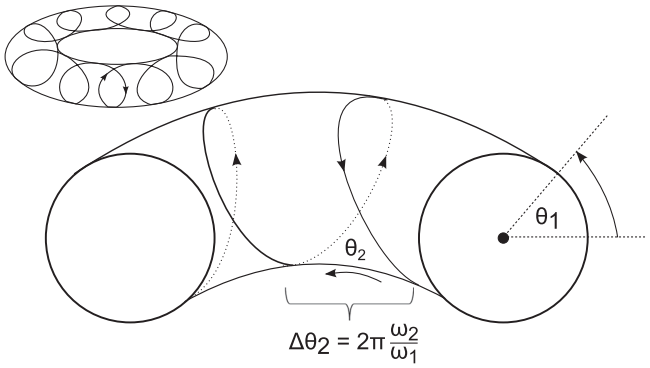


FIG. 1. The orbits in an integrable system with 2 degrees of freedom can be visualized as trajectories wrapping around a two-dimensional torus in phase space with characteristic frequencies $\omega_1$ and $\omega_2$, relating to the angular advances in $\theta_1$ and $\theta_2$. For rational values of $\omega_2/\omega_1 = m/n$ the orbital trajectory will trace out a distinct path, wrapping $n$ times around the $\theta_1$ axis and $m$ times about the $\theta_2$ axis. For irrational values of $\omega_2/\omega_1$ on the other hand a trajectory will fill the surface of the torus densely.

To illustrate this idea for the Kerr metric, consider the reduced Hamiltonian, which is constructed by replacing the conjugate momenta associated with the time and azimuthal symmetries by their constant values to obtain an integrable 2-degree-of-freedom system with an effective potential [16]. The main features of geodesic flow for such a system are sketched in Fig. 1. The trajectory on the torus is described by two characteristic frequencies, associated with the angles $\theta_1$ and $\theta_2$, labeled $\omega_1$ and $\omega_2$, which in the Kerr metric correspond to the radial and longitudinal motions. For rational values of $\omega_2/\omega_1$ the orbit will sample only a finite region of the torus before retracing its own path, while for irrational values of $\omega_2/\omega_1$ a trajectory will fill the torus densely. Orbits with rational frequency ratios involving large integers are very similar to irrational ones; it is only those with small integer ratios that are substantially distinct from the ergodic case.

When describing the astrophysical environment around a black hole such as Sgr A* we need to take into account a number of corrections to the mathematically idealized vacuum Kerr metric. In this case we are interested in the Hamiltonian

$$\mathcal{H} = \mathcal{H}_K + \epsilon \mathcal{H}_1, \tag{1}$$

where $\mathcal{H}_1$ is the perturbing Hamiltonian and $\epsilon$ is a dimensionless parameter characterizing the strength of the perturbation. $\mathcal{H}_1$ contains information about a possible accretion disk [37–39], other sources of matter [40] or dark matter [41,42], structural deviations of the central black hole

[1]Integrability could also break down at a homoclinic orbit, e.g. the last stable orbit discussed in Appendix A. However, this is of less observational interest than the resonances because it marks the transition to the plunge, where the nature of the motion changes drastically.

away from the Kerr metric (i.e. bumpy black hole effects [43–47]), the influence of modified gravity [48,49], or effects of the multipoles of the small mass [19,50,51]. The exact nature of the perturbation does not concern us here. In what follows we simply assume that these modifications are small and represent this by considering the case where $\epsilon \ll 1$.

To quantify the effect of an arbitrary perturbation on the orbital motion and to find the regions where the impact of the perturbation will be greatest, we make use of the KAM theorem [52,53]. The KAM theorem investigates the stability of *near*-integrable systems and suggests that a torus associated with a rational ratio of frequencies will be destroyed in the presence of perturbations. However, provided that the perturbation is small enough, tori for which the ratio of associated characteristic frequencies are *sufficiently irrational* will remain stable and persist, although slightly deformed, in the perturbed Hamiltonian [54,55]. More specifically, consider the vector of frequencies $\omega$ in the unperturbed Hamiltonian and a vector of integers $\mathbf{k}$, and let $d$ denote the dimension of these vectors. The condition for resonance is $\boldsymbol{\omega} \cdot \mathbf{k} = 0$, which can generally be satisfied to arbitrary accuracy by choosing large integers for $\mathbf{k}$. When sufficiently large integers are necessary to satisfy the resonance condition the tori will be preserved, where the definition of *sufficiently* is such that Arnold's criterion holds [52,53]:

$$|\boldsymbol{\omega} \cdot \mathbf{k}| > K(\epsilon)\left(\sum_{i=1}^{d} |k_i|\right)^{-(d+1)}. \tag{2}$$

We will henceforth call $O_{\mathbf{k}} = \sum_{i=1}^{d} |k_i|$ the *order* of the resonance. The factor $K(\epsilon)$ in Eq. (2) approaches zero as the perturbation vanishes, i.e. $\lim_{\epsilon \to 0} K(\epsilon) \to 0$, but its functional form depends on the nature of the perturbation. In a nonintegrable Hamiltonian system, when $\epsilon \lesssim 1$, Eq. (2) suggests a hierarchy of resonant orbits of increasing order whose stability cannot be guaranteed. These are the low-order resonances $1, 1/2, 1/3, 2/3, 1/4, 1/5, 3/4, 2/5, 1/6$. We expect these tori to be destroyed first if the Hamiltonian is perturbed; however, from Eq. (2) we cannot guarantee their destruction either. Changing the Kerr metric's spin parameter is an example of a Hamiltonian perturbation to an integrable Hamiltonian for which none of the lower-order resonant tori is broken.

The destruction of resonant tori corresponds to the physical idea that energy transfer takes place most rapidly if the frequency of the driving force coincides with multiples of the internal frequencies of the system. Similarly, even without a direct input of energy, if a system is deformed the modes that could potentially be altered most are those whose frequencies are rationally related to other modes and which thus have the greatest potential to exchange energy and interact among themselves.

The study of torus destruction is not the subject of this paper. We do however give a heuristic discussion on how to estimate the size of the perturbation required for the onset of strongly chaotic dynamics in Sec. VIII. The detailed calculation will differ depending on the characteristics of the perturbation. The main focus in the following sections is to identify the regions in parameter and physical space where resonant dynamics are likely to occur. If they do occur the KAM theorem limits the impact to low-order resonances.

## III. GEODESIC MOTION IN THE KERR METRIC

### A. Physically motivated constants of motion

The orbital motion of a bound trajectory of two bodies in Newtonian gravity is described completely by an ellipse restricted to a plane. The manner in which this ellipse is traversed is characterized by a single frequency, $\omega_\phi$. A schematic representation of a typical elliptic orbit and the Keplerian variables used to describe it is given in Fig. 2. By

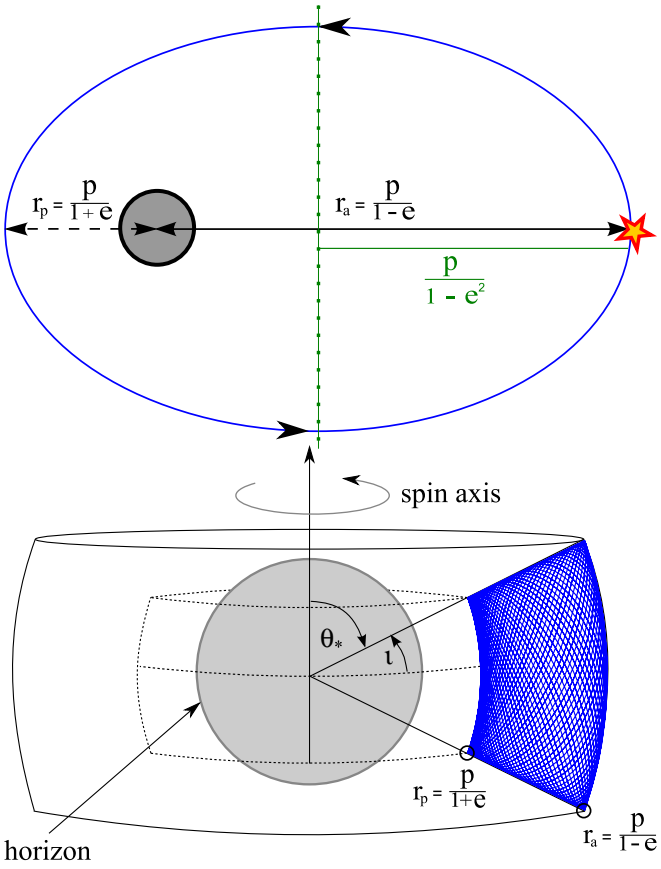


FIG. 2 (color online). Top: Keplerian orbital parameters. The eccentricity, $e$, is a measure of how elliptic the orbit is. When $e = 0$, the orbit is circular; when $e = 1$ the trajectory becomes parabolic. The semilatus rectum, $p$, can be defined in terms of the eccentricity and the semimajor axis of the ellipse as is shown in green in the figure. The point of closest approach $r_p$ is called the *periastron*, while the most outlying point the orbit reaches is the *apastron* denoted by $r_a$. Bottom: The orbital trajectory as shown in three dimensions. The third orbital parameter, namely the maximum inclination angle $\iota = \pi/2 - \theta_*$, is the angle with respect to the black hole's equatorial plane and $\theta_*$ is the minimum Boyer-Lindquist $\theta$ value attained.

contrast in the Kerr metric bound orbits are not restricted to a plane but are confined to a toroidal region whose shape is characterized by the constants of motion, the energy $E$, the $z$-component of angular momentum $L_z$ and Carter constant $Q$. For geodesics in Kerr, the rotational frequency $\omega_\phi$ describing the rotational motion in the azimuthal direction is augmented by two libration-type frequencies $\omega_r$ and $\omega_\theta$ which characterize motion in the radial and longitudinal directions respectively. The bottom panel in Fig. 2 gives a schematic representation of the origin of the $\omega_r$ and $\omega_\theta$ frequencies associated with the orbit.

In the subsequent sections we will explore the location of the resonances for the $\omega_r$ and $\omega_\theta$ frequencies in Boyer-Lindquist coordinates. Instead of using the constants of motion $\{E/\mu, L_z/\mu, Q/\mu^2\}$[2] we will describe the orbits using variables analogous to the Keplerian variables of classical celestial mechanics, namely the eccentricity ($e$), sine of the maximum inclination angle ($\sin\iota = \cos\theta_*$) and semilatus rectum ($p$) as illustrated in Fig. 2. These are defined by writing the periastron or point of closest approach to the central object as $r_p = p/(1+e)$, the apastron or furthest point the trajectory reaches as $r_a = p/(1-e)$ (both in units of the black hole mass) and the turning point of the longitudinal motion as $\theta_*$. The typical frequency of oscillations between $r_a$ and $r_p$ is described by $\omega_r$, whereas the longitudinal oscillations about the equatorial plane, $-(\pi/2-\theta_*) \le \iota \le \pi/2-\theta_*$, are described by $\omega_\theta$.

### B. Equations of motion

For a test mass in orbit around a Kerr black hole the equations governing the radial and longitudinal motion, expressed in Boyer-Lindquist coordinates $(t, r, \theta, \phi)$, are [36]

$$\left(\frac{dr}{d\lambda}\right)^2 = R(r), \qquad \left(\frac{dz}{d\lambda}\right)^2 = \Theta(z), \tag{3}$$

where $z = \cos(\theta)$ and we have chosen to parametrize the orbit in terms of a nonaffine evolution parameter $\lambda = \int d\tau/(r^2 + a^2\cos^2\theta)$, rather than the proper time $\tau$, so that the radial and longitudinal equations decouple (this in fact just corresponds to working in the extended phase space). The radial and longitudinal potentials can respectively be expressed as

$$R = [(r^2+a^2)E - aL_z]^2 - \Delta[\mu^2 r^2 + (L_z - aE)^2 + Q], \tag{4}$$

$$\Theta = Q(1-z^2) - [(\mu^2 - E^2)a^2(1-z^2) + L_z^2]z^2, \tag{5}$$

where $\Delta = r^2 - 2Mr + a^2$ and $a = S/M$ is the spin per unit mass. (We will henceforth use units where $M = 1$.) The $R$ and $\Theta$ potentials are quartic polynomials of their respective arguments and can equivalently be expressed in factored form as

$$R = -\frac{\beta^2}{a^2}(r-r_1)(r-r_2)(r-r_3)(r-r_4) \tag{6}$$

$$\Theta = \beta^2(z^2 - z_-^2)(z^2 - z_+^2) \tag{7}$$

where $\beta^2 = (\mu^2 - E^2)a^2$. In Eq. (6) we label the roots so that $r_1 \ge r_2 \ge r_3 > r_4$ and in Eq. (7) so that $z_+ \ge z_-$. For bound orbits, Eq. (3) dictates that the $r(\lambda)$ and $z(\lambda)$ functions describing the orbital motion oscillate between two of the roots of Eqs. (6) and (7) respectively. The generalized Keplerian variables are defined in terms of the roots of the potential functions as

$$r_1 = \frac{p}{1-e}, \qquad r_2 = \frac{p}{1+e}, \qquad z_- = \cos(\theta_*). \tag{8}$$

When quantifying the resonance behavior in the subsequent sections we would like to express the results entirely in terms of the variables $\{p, e, z_-\}$ rather than using $\{E, L_z, Q\}$. The fact that the roots $r_3, r_4$, and $z_+^2$ cannot be viewed as independent functions but rather must be interpreted as functions of the set of independent variables $\{p, e, z_-\}$ complicates the calculation. By comparing Eqs. (5) and (7) we can find $z_\pm^2$ is given explicitly in terms of $\{E, L_z, Q\}$ as follows:

$$z_\pm^2 = \frac{[(L_z^2 + Q + \beta^2) \pm \sqrt{(L_z^2 + Q + \beta^2)^2 - 4Q\beta^2}]}{2\beta^2}. \tag{9}$$

Equating the coefficients of $r$ in the two expressions for the radial equation, Eqs. (4) and (6), allows us to obtain the following expressions relating the constants $\{E, L_z, Q\}$ to the roots of the factorization

$$\begin{aligned}
\frac{E^2}{\mu^2} &= 1 - \frac{2(1-e^2)}{2p + (1-e^2)\varpi_+}, \\
\frac{L_z^2}{\mu^2} &= \frac{2p(p+2\varpi_+) - 2a^2(1-e^2)}{2p + (1-e^2)\varpi_+} \\
&\quad + \frac{2(a^2(1-e^2) - p^2)\varpi_\times}{a^2(2p + (1-e^2)\varpi_+)}, \\
\frac{Q}{\mu^2} &= \frac{2p^2\varpi_\times}{a^2(2p + (1-e^2)\varpi_+)}
\end{aligned} \tag{10}$$

where we have set $\varpi_+ = r_3 + r_4$ and $\varpi_\times = r_3 r_4$. In addition the condition

$$\begin{aligned}
\frac{2aEL_z}{\mu^2} &= a^2 + \frac{2(\varpi_\times - 2a^2)(1-e^2) - 2p\varpi_\times}{(2p + (1-e^2)\varpi_+)} \\
&\quad \frac{-p^2(\varpi_+ - 2) + 4p\varpi_+}{(2p + (1-e^2)\varpi_+)}
\end{aligned} \tag{11}$$

[2]The rest mass of the probe, $\mu$, is introduced here to ensure the constants of motion are dimensionless.

must also hold. Squaring Eq. (11) and then substituting in the expressions for $E^2$ and $L_z^2$, Eq. (10) results in a quadratic equation for $\varpi_+$ and $\varpi_-$ in terms of $p$ and $e$:

$$\begin{aligned}&\varpi_+\varpi_\times[p(1-e^2)(p+4-a^2)+p^2(p-4)-a^2(1-e^2)^2]\\&\quad+\varpi_\times^2[p+e^2-1]^2+2p\varpi_\times[(p-a^2)(p+e^2-1)]\\&\quad+\frac{1}{4}\varpi_+^2[a^4(1-e^2)^2-2a^2(1-e^2)p(p+4)\\&\quad+(p-4)^2p^2]+p\varpi_+[a^2(1-e^2)(a^2+p)\\&\quad-a^2p(p+4)-(p-4)p^2]+p^2(a^2-p)^2=0.\end{aligned}\tag{12}$$

If $z_-^2\neq 0$ we can use Eqs. (9) and (10) to rewrite $z_+^2$ as

$$z_+^2=\frac{p^2\varpi_\times}{a^4(1-e^2)z_-^2}.\tag{13}$$

We will always treat the $z_-^2=0$ or $Q=0$ limit of orbits restricted to the equatorial plane separately. Using Eqs. (9), (10) and (13) we can further show that

$$2a^2p\varpi_+z_-^2=(a^2(1-e^2)z_-^2-p^2)(a^2z_-^2-\varpi_\times).\tag{14}$$

Equation (14) is a linear condition in $\varpi_+$ and $\varpi_\times$ which, in conjunction with (12), implicitly determines $\varpi_+(p,e,z_-)$ and $\varpi_\times(p,e,z_-^2)$ and thus the roots $r_3$ and $r_4$ in terms of $\{p,e,z_-\}$. Substituting Eq. (14) into (12) eliminates $\varpi_+$ and yields a quadratic equation in $\varpi_\times$. As a result a closed-form expression can easily be found for $\varpi_\times$ and subsequently $\varpi_+$. We will not give the expressions here and continue to work with the implicit quantities $\varpi_+$ and $\varpi_\times$, substituting their actual values only at the end of the calculations. The two solutions that result from the quadratic equation can be interpreted as test masses that either corotate or counter-rotate with respect to the spin, $a$, of the black hole. Orbits that corotate with the black hole ($L_z$ has the same sign as $a$) are called *prograde* and those that counter-rotate ($L_z$ has the opposite sign to $a$) are *retrograde* orbits. For a given $\{p,e,z_-\}$ the prograde orbit's angular momentum is higher than that of the retrograde orbit. On the other hand prograde orbits have lower orbital energy than their retrograde counterparts [28].

One special set of orbital parameters is the case when the roots satisfy $r_3=r_2$, which corresponds to the innermost stable orbit (ISO) separating stable bound orbits from those that plunge into the black hole. For a given eccentricity and longitudinal parameter $z_-$ the semimajor axis satisfying this condition demarcates the smallest value of $p$ at which a stable bound orbit can exist. We shall explicitly solve for the ISO for all values of $a$, $e$ and $z_-$ in Appendix A and use it as a comparative benchmark for the location of resonant orbits in the subsequent sections.

## IV. THE RESONANCE CONDITION

In this section we begin to characterize the orbits which will exhibit resonant behavior. We are interested in the parameter values for which $\omega_r$ and $\omega_\theta$ are commensurate. Given relatively prime integers $m$ and $n$ we seek the surface in the three-dimensional parameter space spanned by $p$, $e$ and $z_-$ where

$$m\omega_r=n\omega_\theta.\tag{15}$$

This is equivalent to saying that the time it takes the longitudinal motion to traverse exactly $n$ times between its turning points is equal to the time it takes the radial motion to traverse $m$ times between its turning points. For Kerr geodesics $m\geq n$ since the radial frequency is always the smallest of the three frequencies. This translates into the following integral condition

$$m\int_{-z_-}^{z_-}\frac{dz}{\sqrt{\Theta}}=n\int_{r_2}^{r_1}\frac{dr}{\sqrt{R}}.\tag{16}$$

Substituting Eqs. (6) and (7) we find that this is equivalent to the condition

$$\begin{aligned}an\int_{r_1}^{r_2}\frac{dr}{\sqrt{(r_1-r)(r-r_2)(r-r_3)(r-r_4)}}\\=-m\int_{-z_-}^{z_-}\frac{dz}{\sqrt{(z^2-z_-^2)(z^2-z_+^2)}}.\end{aligned}\tag{17}$$

The subject of the rest of the paper is to characterize the solutions to this equation. The strategy is to express both the radial and longitudinal integrals in their most symmetric form using Carlson's integrals [33–35]. Carlson's integral of the first kind is defined to be

$$R_F(\alpha,\beta,\gamma)=\frac{1}{2}\int_0^\infty\frac{dt}{\sqrt{(t+\alpha)(t+\beta)(t+\gamma)}}.\tag{18}$$

In Appendix B we list a number of identities and rapidly converging approximation techniques that make Carlson's integrals a valuable analytic tool for characterizing the resonant surfaces. Using Eq. (B2) of Appendix B we can rewrite Eq. (17) as

$$\begin{aligned}&anR_F(0,(r_2-r_3)(r_1-r_4),(r_2-r_4)(r_1-r_3))\\&\quad=-mR_F(0,(z_-+z_+)^2,(z_--z_+)^2).\end{aligned}\tag{19}$$

This expression can be further simplified using the identity (B8) to rewrite the right-hand side and the fact that the equations are homogeneous (B6) to absorb the constant factor. We shall refer to the resulting equation,

$$R_F(0,(r_2-r_3)(r_1-r_4),(r_2-r_4)(r_1-r_3)) = R_F(0,\kappa a^2(z_+^2-z_-^2),\kappa a^2 z_+^2), \tag{20}$$

as *the resonance condition* and explore its properties by studying various limiting cases. In this expression we have defined the parameter $0<\kappa<1$ to indicate which resonance we are considering,

$$\kappa = \frac{n^2}{m^2}. \tag{21}$$

In the subsequent section we will explore all the qualitative features of a resonance by examining an easily evaluated approximation to Eq. (20) for large $p$. We then give a number of formulas valid in the region near the black hole in special cases.

## V. SOLUTIONS TO THE RESONANCE CONDITION

When seeking solutions of Eq. (20) it is convenient to rewrite it in terms of a rapidly converging series. This series allows us to identify the three important parameters in the problem. The first sets the overall scale and a rough location of the resonance. The remaining two are expansion parameters $<1$ that determine the more subtle structure of the resonance surface. We give explicit expressions for these parameters in terms of the variables introduced in Sec. III B. Next, we evaluate the series in the large $p$ limit to obtain a simple analytic model which illustrates the important features of any resonance. We then turn to the astrophysically more interesting strong field region where the low-order resonances occur and give a number of exact analytic formulas for special cases. We conclude the section by numerically computing the detailed behavior of the $2/3$ resonance and compare our analytic results and approximations to the numerical solutions.

### A. General series expansion

The resonance condition (20) can be rewritten in the form

$$R_F(0,y_1+\delta_1,y_1-\delta_1) = R_F(0,\kappa(y_2+\delta_2),\kappa(y_2-\delta_2)), \tag{22}$$

where

$$y_1 = \frac{p^2-p(r_3+r_4)}{1-e^2}+r_3r_4, \qquad \delta_1 = \frac{ep(r_4-r_3)}{1-e^2},$$
$$y_2 = \frac{a^2}{2}(2z_+^2-z_-^2), \qquad \delta_2 = -\frac{a^2z_-^2}{2}. \tag{23}$$

It will be shown below Eq. (25) that $\delta_i/y_i \ll 1$ for all physically interesting parameters. As a result, each side of Eq. (22) can be expanded in $\delta_i \ll y_i$, using the rapidly converging series of Eq. (B10). Squaring the resulting expansions, moving all the terms containing the small parameters $\delta_i/y_i$ to one side, and reexpanding the result, we obtain the equation

$$\frac{y_1}{\kappa y_2} = 1+\frac{3}{8}\left(\frac{\delta_1^2}{y_1^2}-\frac{\delta_2^2}{y_2^2}\right)-\frac{9}{64}\frac{\delta_1^2\delta_2^2}{y_1^2y_2^2} + \frac{123}{512}\left(\frac{\delta_1^4}{y_1^4}-\frac{\delta_1^4}{y_1^4}\right)+O\left(\frac{\delta^6}{y^6}\right). \tag{24}$$

In terms of the variables introduced in Sec. III B, the three quantities that enter the expansion of the resonance condition (24) are

$$\frac{y_1}{y_2} = \frac{2a^2z_-^2((1-e^2)\varpi_\times+p^2-p\varpi_+)}{(a^4(e^2-1)z_-^4+2p^2\varpi_\times)},$$
$$\frac{\delta_1}{y_1} = \frac{-ep\sqrt{\varpi_+^2-4\varpi_\times}}{(1-e^2)\varpi_\times+p^2-p\varpi_+},$$
$$\frac{\delta_2}{y_2} = \frac{(1-e^2)a^4z_-^4}{(1-e^2)a^4z_-^4-2p^2\varpi_\times}. \tag{25}$$

The first term $y_1/y_2$ ultimately sets the overall scale of $p$ at which a particular resonance occurs. Recall that the parameters $\{z_-,e,a,\kappa\}\in[0,1]$. By examining Eq. (25) one can further verify that the $\delta_i/y_i$ terms are always less than unity ensuring the convergence of the series in Eq. (24). The parameters $\delta_1/y_1$ and $\delta_2/y_2$ vanish when $e=0$ and $z_-=0$ respectively. The special limiting case when both these conditions hold allows us to find an exact analytic result that is valid in all regions of the spacetime. We shall examine this special case in Sec. V C. However before we do so, it is instructive to examine the properties of resonances that occur at large $p$ values. The features we explore in this limit qualitatively capture the characteristics of resonances in general.

### B. Anatomy of a resonance in the weak field limit $p\to\infty$

In the weak field limit, when $p\to\infty$, the dominant terms in the expansion of $\varpi_\times$ and $\varpi_+$ found by solving Eqs. (14) and (12) are

$$\varpi_\times = a^2z_-^2\left(1+\frac{4}{p}\pm\frac{8a\sqrt{(1-z_1^2)}}{p^{3/2}}\right)+O\left(\frac{1}{p^2}\right),$$
$$\varpi_+ = 2+\frac{8+2a^2(1-z_-^2)}{p}\pm4a\sqrt{\frac{1-z_-^2}{p}}\left(1+\frac{6}{p}\right)+O\left(\frac{1}{p^2}\right). \tag{26}$$

Substituting Eq. (26) into Eq. (25) and simplifying the result gives the dominant behavior of the three essential parameters in the resonance condition

$$\frac{y_1}{y_2} = 1 - \frac{6}{p} \mp \frac{12a\sqrt{1-z_-^2}}{p^{3/2}} - \frac{3a^2((e^2-5)z_-^2+4)}{2p^2} + O\left(\frac{1}{p^{5/2}}\right), \tag{27}$$

$$\frac{\delta_1}{y_1} = -\frac{2e\sqrt{1-a^2z_-^2}}{p} \mp \frac{4ae}{p^{3/2}}\sqrt{\frac{z_-^2-1}{a^2z_-^2-1}} + O\left(\frac{1}{p^2}\right)$$
$$\frac{\delta_2}{y_2} = -\frac{a^2(1-e^2)z_-^2}{2p^2} + O\left(\frac{1}{p^3}\right). \tag{28}$$

The small $\delta_1/y_1$ and $\delta_2/y_2$ parameters scale with $1/p$ and $1/p^2$ respectively indicating that they become almost negligible for large $p$ and reaffirming the choice of $\delta_i$ as an expansion parameter.

To illustrate the basic properties of the resonance condition we substitute Eqs. (27) and (28) into Eq. (24) and keep terms up to $O(p^{-2})$. The resulting approximate resonance condition,

$$\pm 24a\sqrt{p(1-z_-^2)} = 2p^2(\kappa-1) + 12(p+a^2) + 3e^2\kappa - 3a^2z_-^2(e^2(\kappa-1)+5), \tag{29}$$

is valid for large $p$ values only. However, this weak field approximation demonstrates all the qualitative properties of resonant surfaces and gives a good approximation even relatively close to the black hole. The precise manner in which Eq. (29) breaks down for low-order resonances is numerically explored in Sec. V E.

To build our intuition of the typical features of resonant surfaces and their dependence on the parameters $a, e, z_-, \kappa$ and $p$ we analyze Eq. (29) in detail. For quasicircular orbits and vanishing black hole spins $(a, e) \to 0$, the resonances occur at

$$p^* = p(a=0, e=0, z_-, \kappa) = \frac{6}{1-\kappa}. \tag{30}$$

For a given $\kappa$, this value of $p^*$ sets the general mean radius in physical space (measured in units of $GM/c^2$) about which all the interesting features of a resonance occur. This is a robust result that remains an exact analytic solution even in the region near the horizon, as we will prove in Sec. V C. For a fixed integer $m$, resonances with $\kappa = [(m-1)/m]^2$ correspond to the maximum resonance radius given by $p = 6m^2/(2m-1)$. Resonances with $n < m-1$ occur at a radius less than that associated with $n = m-1$. The maximum $p$ associated with a denominator $m$ thus scales linearly with $m$ for large values of $m$.

In the limiting case $a \to 0$ the dependence on eccentricity is

$$p(a=0, e, z_-, \kappa) = \frac{p^*}{2}\left(1 + \sqrt{1 + e^2\left(\frac{p^*-6}{p^{*2}}\right)}\right). \tag{31}$$

Since $e \le 1$ and $p^* > 6$ we see that the effect of eccentricity on the resonance location is small. We also observe that in the case $a \to 0$ the location of the resonance becomes independent of $z_-$.

We now examine the general spinning case. Squaring both sides of Eq. (29) results in a polynomial condition that is quartic in $p$ and quadratic in $z_-^2$. We choose to analyze the solution surface by specifying the $z_-^2 = z_-^2(a, e, p, \kappa)$ for a fixed $\kappa$ rather than explicitly working with the quartic roots associated with $p$. The appropriate expression for $z_-^2$ is

$$z_-^2 = \frac{4a^2 + e^2 - \frac{6e^2+4p^2}{p^*}}{a^2(5-\frac{6e^2}{p^*})} - \frac{12p(\frac{2e^2}{p^*}+1)}{a^2(5-\frac{6e^2}{p^*})^2} + \frac{8}{a^2}\sqrt{\frac{p[a^2-e^2+\frac{6e^2(1-a^2)+4p^2}{p^*}]}{(5-\frac{6e^2}{p^*})^3} - \frac{4p^2(1-\frac{6e^2}{p^*})}{(5-\frac{6e^2}{p^*})^4}}. \tag{32}$$

This function is depicted in Fig. 3 for a fixed spin parameter of $a = 9/10$ and integer ratio $\kappa = (9/10)^2$. It has the shape of a parabolic arch centered around $p^* \approx 31.6$. Furthermore, the qualitative features that will be discussed here are characteristic for all resonances. The function given in Eq. (32) has a maximum value of $z_-^2 = 1$ which occurs when $p_{\rm polar} = p(a, e, z_- = 1, \kappa)$ has the value

$$\frac{p_{\rm polar}}{p^*} = \frac{1}{2}\left(1 + \sqrt{1 + \frac{(e^2-a^2)}{p^*} - \frac{6(1-a^2)e^2}{p^{*2}}}\right). \tag{33}$$

Since $\{e, a\} \in [0, 1]$ and $p^* \gg 8$, the maximum only deviates by a few percent from the $p^*$ value as the spin and eccentricity deviate from zero. The analytic value of the maximum given by Eq. (33) is plotted as a dark line in Fig. 3. When $z_-^2 < 1$ there are two possible values of $p$ that lie on the resonance sheet for a given eccentricity: the resonance for a retrograde orbit $p_- > p_{\rm polar}$ and the resonance for a prograde orbit which occurs closer to the black hole $p_+ < p_{\rm polar}$. The sign in the naming convention of retrograde and prograde orbits relates to the sign of the product of the angular momentum and the spin of the black hole ($aL_z$), and not the orbit's relative position with respect to $p_{\rm polar}$.

As $z_-$ decreases and the resonance surface moves from the polar towards the equatorial region, the influence of spin becomes increasingly important and the distance $p_-$ to $p_+$ monotonically increases. The expression for $p_-$ and $p_+$ can easily be found in closed form by substituting $z_- = 0$ into Eq. (29) and solving the resulting quartic for $p$. However, since the results are messy and add little to the discussion we do not give the general results explicitly and merely plot these curves in Fig. 3. To benchmark the size of the arch we consider the limit of vanishing eccentricity and inclination and obtain

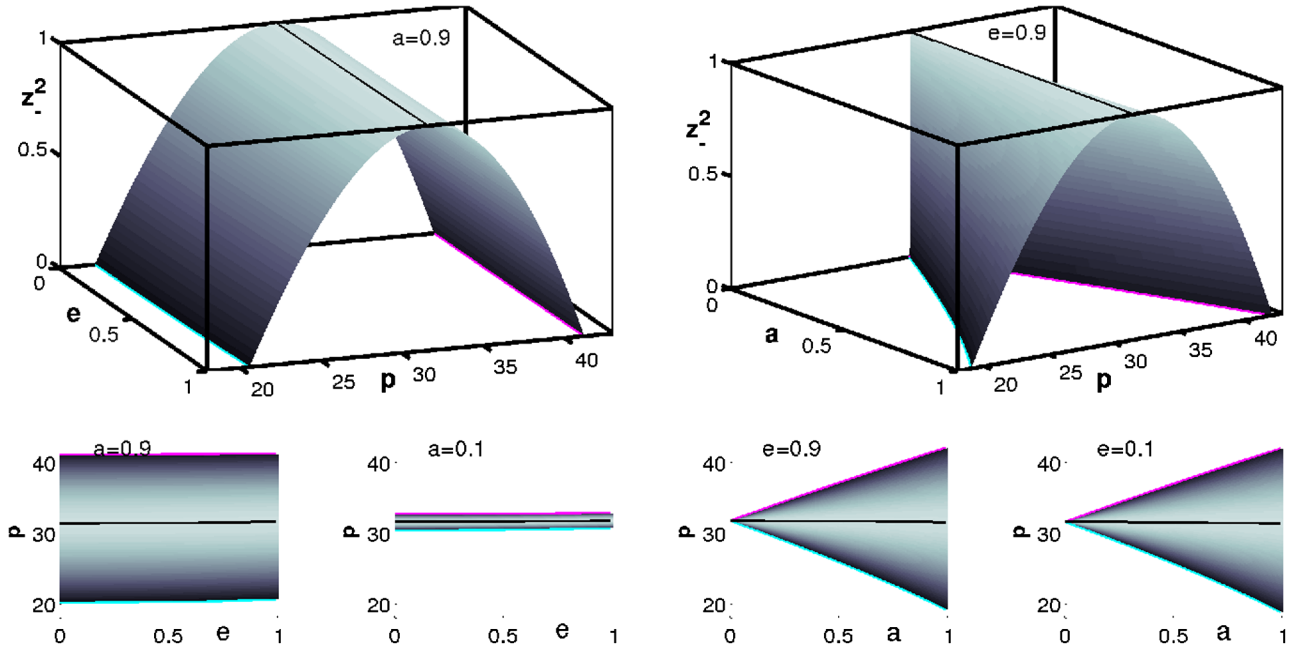


FIG. 3 (color online). Graphical representation of the approximate resonance condition (29) or equivalently (32) plotted for the $\kappa = (9/10)^2$ resonance. The eccentricity dependence is shown in the three plots on the left. The top left plot displays the typical arch shape seen for all resonances. Here the arch is centered around $p^* \approx 31.6$ reaching a maximum value of $z_- = 1$ at $p = p_{\rm polar}$ given in Eq. (33) and indicated by a dark line on the plot. The lines where arches intersect the $z_- = 0$ plane are indicated in magenta (right) and cyan (left) and show the maximum (retrograde) and minimum (prograde) values $p$ attains for a fixed $e$. Note that the resonance shape for a fixed spin is very weakly dependent on the eccentricity of the orbits. The spin dependence of the approximate resonance condition is shown in the three plots on the right for $e = 1/10$ and $e = 9/10$. Observe that as $a \to 0$ the arch pinches off to a line at $p = p_{\rm polar}$, Eq. (33). The maximum arch width occurs for a maximally spinning black hole $a = 1$ as predicted by Eq. (34).

$$\frac{p_\pm(a, e = 0, z_- = 0, \kappa)}{p^*} = \frac{1}{2}\left(1 + \sqrt{1 \mp \frac{4a}{\sqrt{p^*}}} \mp \frac{2a}{\sqrt{p^*}}\right). \tag{34}$$

The maximum span of the arch occurs for a maximally spinning black hole, $a = 1$. For lower spin values a good approximation of the span of the arch is $(p_- - p_+) \approx 4a\sqrt{p^*}(1 + a^2/p^*)$. The lowest-order correction to Eq. (34) with respect to eccentricity is $e^2(p^* - 6)/(4p^{*2})$ and is the same for both pro- and retrograde orbits.

Having thus explored the basic features of a resonance for a given spin parameter $a$ and observed the weak dependence of these features on eccentricity, we will now choose a representative eccentricity and then study the spin dependence. The right-hand three panels of Fig. 3 show the $\kappa = (9/10)^2$ resonance surface for eccentricity values of $e = 9/10$ and $1/10$ as a function of black hole spin and $p$. As predicted by Eq. (34) the arch width exhibits a strong spin dependence. The arch's inverted "$U$" profile pinches off to a single column "$I$" profile at $p = p_{\rm polar}$ [Eq. (33)] when $a \to 0$. This indicates that resonances in the nonspinning limit become independent of inclination because the longitudinal frequency degenerates to the $\phi$-frequency in this case. As the black hole's spin increases from zero the opening width of the arch between the pro- and retrograde branches increases until a maximum arch width is attained at $a = 1$. The result is a "$V$"-shaped footprint of the arch in the $p - a$ plane, with the $V$ profile's vertex corresponding to $a = 0$. The inclination dependence of the resonance surfaces can simply be characterized as the monotonic closing off of the $V$ profile's pro- and retrograde branches with increasing inclination until they merge into a single line forming the arch's spine at $p_{\rm polar}$.

This completes our discussion of resonances in the weak field limit. The features described here and the $U$-$V$-$I$ transitions are characteristic of all resonances. The actual values of the resonant surface of the true resonance condition begin to deviate from our weak field model as the black hole is approached. The largest deviation occurs in the equatorial limit, where the effect of spin is most marked. In the polar regions, the weak field resonance condition remains a remarkably accurate approximation to the true resonance surface. In Sec. V E we numerically characterize several low-order resonances and provide a quantitative comparison with the approximate results obtained in this section.

As we shall see next, in the strong field region it is possible to obtain exact analytic results for the $V$ equatorial footprint for $e = 0$. Since the resonant surface depends very weakly on $e$ this result is a good indicator for all resonant behavior.

### C. Exact solutions to the resonance condition in special cases

In this section we explore easily evaluated exact solutions to the resonance condition of Eq. (20) that can be used to characterize the resonant behavior near the black hole. The case we will consider first is the limit of circular equatorial orbits, i.e. $e \to 0$ and $z_- \to 0$. As remarked in Sec. V A this case sets the parameters $\delta_1/y_1 = \delta_2/y_2 = 0$ in Eq. (22) and thus a valid solution to the resonance condition is found when

$$\frac{y_1}{y_2} = \kappa. \tag{35}$$

Note that in evaluating this case we will not be resorting to Eq. (25) that was derived using Eq. (13) which assumed that $z_-^2 \neq 0$. Instead we return to Eq. (9) and observe that $z_- = 0$ if and only if $Q = 0$. By Eq. (10) we see that $Q = 0$ implies $\varpi_\times = 0$. The simplified version of Eq. (10) is

$$\frac{E^2}{\mu^2} = 1 - \frac{2}{2p + \varpi_+}, \qquad \frac{L_z^2}{\mu^2} = 4p - 2\frac{a^2 + 3p^2}{2p + \varpi_+}. \tag{36}$$

Substituting Eq. (36) into Eq. (9) gives an expression for $z_+$,

$$z_+^2 = \frac{p(p + 2\varpi_+)}{a^2}. \tag{37}$$

Setting $\varpi_\times = 0$ in Eq. (11) results in a quadratic equation for $\varpi_+$ which has the following roots,

$$\varpi_+ = \frac{2p(a \pm \sqrt{p})^2}{p(p-4) - a^2 \mp 4a\sqrt{p}}. \tag{38}$$

We are now in a position to evaluate Eq. (35) which becomes

$$\frac{y_1}{y_2} = \frac{p(p - \varpi_+)}{a^2 z_+^2} = \frac{p - \varpi_+}{(p + 2\varpi_+)} = \kappa. \tag{39}$$

Inserting the value for $\varpi_+$ from Eq. (38) leads to

$$\kappa = \frac{(p-6)p - 3a^2 \pm 8a\sqrt{p}}{p^2 + 3a^2 \mp 4a\sqrt{p}}, \tag{40}$$

where the upper (lower) sign corresponds to prograde (retrograde) orbits. This result can alternatively be obtained from the frequencies of linear perturbations to circular equatorial orbits [56,57]. An equivalent way of expressing Eq. (40) is in terms of the quartic polynomial:

$$[p(p - p^*) - a^2(p^* - 3)]^2 - 4a^2 p(p^* - 2)^2 = 0. \tag{41}$$

In the above expression we chose to use $p^* = 6/(1 - \kappa)$ to identify the resonance rather than $\kappa$ itself. This choice makes it obvious that in the nonspinning limit $p = p^*$ is an analytic solution to the resonance condition.

Equation (41) is a key result of this paper because it characterizes the exact $V$ profile of all resonances for $z_- \to 0$ as a function of spin. As discussed in Sec. V B on the weak field limit, eccentricity has very little effect on the resonance surface and inclination merely deforms the $V$ profile into a line as $z_- \to 1$. This single formula thus allows us to characterize all resonant effects of arbitrarily spinning black holes.

To efficiently evaluate Eq. (41) it is useful to view it as a quadratic polynomial in $a^2$ instead of a quartic polynomial in $p$. Solving for $a^2$ in terms of $p$ and $p^*$ leads to

$$a_*^2(p) = \frac{p^2(p^* - 3) + p(p^{*2} - 5p^* + 8)}{(p^* - 3)^2} + \frac{-2p(p^* - 2)\sqrt{p(p^* - 3) - p^* + 4}}{(p^* - 3)^2}. \tag{42}$$

We use Eq. (42) to plot the spin dependence of the $V$ profile for $z_- = 0$ for several low-order resonances in Fig. 4.

The maximum splitting of the retrograde and prograde branches of the $V$ occurs when $a = 1$; in this case the relevant roots of Eq. (41) are

$$p_\pm = p^* - 1 \mp 2\sqrt{p^* - 2}. \tag{43}$$

The maximum opening distance of the $V$ profile is then

$$(p_- - p_+) = 4\sqrt{p^* - 2}. \tag{44}$$

Even though Eq. (41) can readily be solved for $p$, the expression is complicated and it is often difficult to identify which roots correspond to the retrograde and prograde branches; we thus provide a useful series expansion. For low spin values, the solutions to Eq. (41) admit the expansion

$$p_\mp = p^* \pm \frac{2a(p^* - 2)}{\sqrt{p^*}} - \frac{a^2(p^{*2} - 5p^* + 8)}{p^{*2}} \pm \frac{a^3(p^* - 2)(2p^{*2} - 11p^* + 20)}{p^{*7/2}} + O(a^4). \tag{45}$$

Table I summarizes the numerical values associated with the low-order resonances depicted in Fig 4, both in dimensionless and physical units for the special case of the Galactic center, Sgr A*. Lower-order resonances, shown in bold in this table, are likely to have observationally detectable dynamics. According to the KAM theorem these tori, when perturbed, are most likely to be disrupted and the ensuing rapid changes in the orbital parameters should have a dramatic effect when compared to the systematic smooth distortion of perturbation induced effects away from resonant orbits. We will discuss this further in Sec. IX. In Sec. V E we give a numerical characterization of several of the lower-order resonances

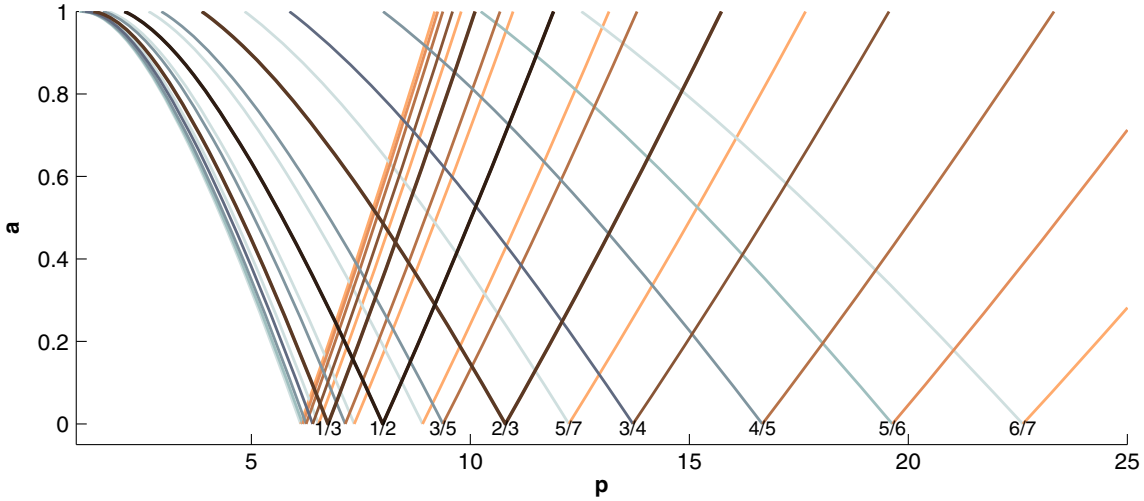


FIG. 4 (color online). The location of orbits with resonant frequencies in the limiting case of $e = 0$ and $z_- = 0$ as a function of spin, $a$ and semilatus rectum, $p$ [7]. Resonances are labeled at their vertex by the rational ratio $n/m$. All resonances with $m \leq 7$ are shown. For $a = 0$ the prograde and retrograde branches are degenerate at $p = p^*$, as the spin increases the retrograde branch leans right (copper tinge) and the prograde branch leans left (blue tinge). In general lower-order resonances are colored more darkly than their higher-order counterparts. Note the accumulation of resonances as the strong field region is approached.

introduced here. However before we turn to the numerical solution we analytically quantify the effect of eccentricity in greater detail.

### D. Quantifying the effect of eccentricity

To quantify the effect of eccentricity, we consider the limiting case of polar orbits with

$$z_-^2 = 1, \qquad L_z = 0, \qquad z_+^2 = \frac{Q}{\beta^2} = \frac{p^2\varpi_\times}{a^4(1-e^2)}. \tag{46}$$

This choice puts us at the top of the inverted $U$ where the effects of spin are minimal. In this case we can solve Eqs. (12) and (14) for $\varpi_\times$ and $\varpi_-$. Since $L_z$ is zero Eq. (12) reduces to a linear equation. As a result, only one solution

TABLE I. Time and length scales associated with low-order resonances depicted in Fig. 4. This table gives the values for the $e = 0$, $a = 0$, $z_- = 0$ vertices seen in Fig. 4, first in dimensionless units and subsequently in physical units for the special case of the Galactic center, Sgr A*. Lower-order resonances, shown in bold in this table, are most likely to have observationally detectable dynamics.

| Resonance | Location $(GM/c^2)$ | Spin splitting | Period $(GM/c^3)$ | Galactic | center: | Sgr A* |
|---|---|---|---|---|---|---|
| $\sqrt{\kappa} = n/m$ | $p^* = 6/(1-\kappa)$ | $\mathrm{Max}[(p_1 - p_+)/p*]$ | $T = 2\pi p^{*3/2}$ | $p*$ ($\mu$as) | $T$ (min) | $f$ ($10^{-4}$ Hz) |
| ISCO | 6 | 1.33 | 92.3 | 30.6 | 32.7 | 5.10 |
| **1/2** | **8** | **1.22** | **142.1** | **40.9** | **50.3** | **3.31** |
| **1/3** | **27/4 = 6.8** | **1.29** | **110.2** | **34.5** | **39.0** | **4.27** |
| **2/3** | **54/5 = 10.8** | **1.10** | **223.0** | **55.2** | **78.9** | **2.11** |
| 1/4 | 32/5 = 6.4 | 1.31 | 101.7 | 32.7 | 36.0 | 4.63 |
| 3/4 | 96/7 = 13.7 | 1.00 | 319.1 | 70.1 | 112.9 | 1.48 |
| 1/5 | 25/4 = 6.3 | 1.32 | 98.2 | 31.9 | 34.7 | 4.80 |
| 2/5 | 50/7 = 7.1 | 1.27 | 119.9 | 36.5 | 42.4 | 3.93 |
| 3/5 | 75/8 = 9.4 | 1.16 | 180.4 | 47.9 | 63.8 | 2.61 |
| 4/5 | 50/3 = 16.7 | 0.92 | 427.5 | 85.1 | 151.3 | 1.10 |
| 1/6 | 216/35 = 6.2 | 1.32 | 96.3 | 31.5 | 34.1 | 4.89 |
| 5/6 | 216/11 = 19.6 | 0.86 | 546.7 | 100.3 | 193.5 | 0.86 |
| 1/7 | 49/8 = 6.1 | 1.33 | 95.2 | 31.3 | 33.7 | 4.94 |
| 2/7 | 98/15 = 6.5 | 1.30 | 104.9 | 33.4 | 37.1 | 4.49 |
| 3/7 | 147/20 = 7.4 | 1.26 | 125.2 | 37.5 | 44.3 | 3.76 |
| 4/7 | 98/11 = 8.9 | 1.18 | 167.1 | 45.5 | 59.1 | 2.82 |
| 5/7 | 49/4 = 12.3 | 1.05 | 269.4 | 62.6 | 95.3 | 1.75 |
| 6/7 | 294/13 = 22.6 | 0.80 | 675.8 | 115.5 | 239.1 | 0.70 |

exists as is expected because the retrograde and prograde branches should coincide for polar orbits.

Here to illustrate the effect of eccentricity we only give the results in the $a = 0$ limit, since the expressions for $a \neq 0$ are unwieldy, so that

$$\varpi_\times = 0, \qquad \varpi_+ = \frac{2p}{p-4}. \tag{47}$$

Substituting these values into Eq. (25) gives expressions for the parameters that enter into the series expansion of Eq. (24),

$$\frac{y_1}{y_2} = \frac{p-6}{p}, \qquad \frac{\delta_1}{y_1} = -\frac{2e}{p-6}, \qquad \frac{\delta_2}{y_2} = 0. \tag{48}$$

We now reexpand the series in Eq. (24) and substitute Eq. (48) to obtain an explicit expression for $\kappa$,

$$\kappa = (1-6/p)\left(1 - \frac{3e^2}{2(p-6)^2} - \frac{51e^4}{32(p-6)^4} + O(e^6)\right).$$

Inverting this series expansion we find that the dominant behavior of the resonance's dependence on eccentricity is

$$p = p^*\left(1 + \frac{e^2}{4(p^*-6)} - \frac{e^4(4p^*-17)}{64(p^*-6)^3} + O(e^6)\right). \tag{49}$$

The expansion given in Eq. (49) is valid in the strong field region. Note that as the resonant surfaces approach the innermost stable circular orbit (ISCO) ($p = 6$) the effects of eccentricity become increasingly important.

### E. Detailed numerical characterization of low-order resonances

Having studied the resonances in limiting cases, we now provide a full numerical characterization of the properties of the low-order resonances and a comparison with the analytic formulas. We quantify the error in using the weak field approximation of Sec. V B for low-order resonant surfaces and confirm the veracity of the exact analytic solutions found for special cases in the strong field regime.

We calculated the location of the resonances numerically by means of two methods. The first method directly uses the closed-form general expressions for the fundamental frequencies presented by Schmidt [28] [see for example Eqs. (33) and (34) where the frequencies are given in terms of elliptic integrals]. These formulas are not well defined for the limiting cases $e = 0$ and $z_- = 1$ which require explicit modifications [28]. The integrals also become indeterminate when reducing to $a = 0$ or $a = 1$. A careful numerical treatment in the limiting cases ($e = 0, z_- = 0$), where the numerical values are calculated using the procedure presented in Appendix B of [28], recovers the analytic values predicted by Eqs. (42) and (49) to within $\lesssim 0.01\%$ over the entire range of the remaining parameters.

The accuracy of the agreement in these cases is limited by the numerical procedure, e.g. taking $a = 0.005$ and $z_- = 0.99995$ instead of 0 and 1 respectively.

The second semianalytic scheme that we implemented exploits the analytic development of Secs. III B and IV to reduce the computational cost in the following way. The resonance condition Eq. (22) is recast in terms of the three parameters that appear in the series expansion of Eq. (25) as

$$\frac{\omega_r}{\omega_\theta} = \sqrt{\kappa} = \sqrt{\frac{y_1}{y_2}}\frac{R_F(0, 1+\frac{\delta_2}{y_2}, 1-\frac{\delta_2}{y_2})}{R_F(0, 1+\frac{\delta_1}{y_1}, 1-\frac{\delta_1}{y_1})}. \tag{50}$$

For a given $a, e, z_-^2 > 0$ we calculate the values of $p$ that lie on the resonance surfaces by first finding an expression for $\varpi_+$ in terms of $\varpi_\times$ using Eq. (14) and substituting this into Eq. (12). Solving the resulting quadratic for $\varpi_\times$ yields two choices for $\varpi_\times(p)$, corresponding to the prograde and retrograde solutions. Having expressed $\varpi_\times$ and thus $\varpi_+$ in terms of $p$ we can write the three parameters in Eq. (25) as explicit functions of $p$. The right-hand side of Eq. (50) can be evaluated for a given $p$ by repeatedly applying the relation (B8) which tends to make the two arguments in the $R_F(0, x^2, y^2)$ function equal (five iterations usually suffice to reach machine precision) and then using (B7) to yield the result; alternately one can use Eq. (B12) to express Carlson's $R_F$ functions as elliptic integrals of the first kind. A line search method can then be used to find a value $p$ that solves (50) for a given $\kappa$, using $p = p*$ as the first guess. This method has yielded accurate results for all parameter values except in the equatorial case $z_- = 0$. The cases $e = 0$, $z_- = 1$, $a = 0$ and $a = 1$ do not require special treatment, in contrast to the first direct numerical method. The special case of $z_- = 0$ can be treated analytically, as was shown in the previous sections. The results computed with this semianalytical method are in complete agreement with those obtained by the direct numerical method. This serves as an independent check of our computations. We note, however, that the computational costs for the semianalytic method are substantially lower than for the direct method.

In the numerical investigation shown in Figs. 5 and 6 we sample the parameter space by choosing several values of $e$ and $z_-$ in the range (0,1) and numerically solve the equation $\omega_r/\omega_\theta = 1/2, 2/3$ or $3/4$ for $p$, given a fixed spin value $a$. Figure 5 shows several surfaces or sheets corresponding to different black hole spins. The sheets are plotted on the $\{e, p, z_-^2\}$ coordinate axis to make the correspondence to Fig. 3 clear. The blue sheets $(a)$–$(c)$ indicate the location of prograde orbits. The spin value is decreased from sheet $(a)$ to $(c)$. The red sheets indicate retrograde orbits with spin values increasing from $(d)$ to $(f)$. The higher the eccentricity, the further out in $p$ the resonances occur. The more inclined the orbital plane, the further out (closer in) the resonances for prograde (retrograde) orbits occur. These qualitative features are the same as those identified in the

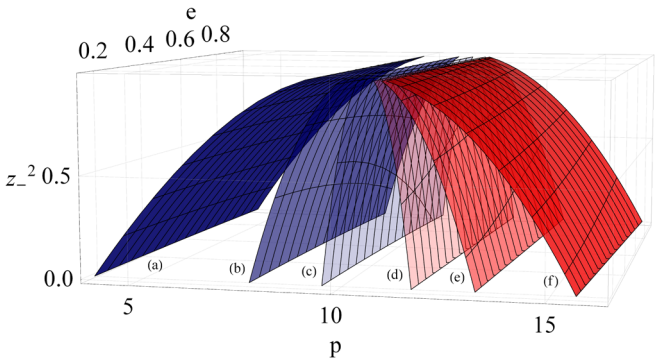


FIG. 5 (color online). Numerically computed surfaces for the 2/3 resonance. Prograde orbits are shown in blue (left) for spin values (a) 0.99, (b) 0.5 and (c) 0.2. Retrograde orbits are shown in red (right) for spin values (d) 0.2, (e) 0.5 and (f) 0.99.

weak field limit in Sec. V B. Since the value of the orbital eccentricity has the smallest impact on the location of the resonance, we subsequently choose a representative eccentricity and explore the spin dependence for several low-order resonances. In Fig. 6 the $1/2$, $2/3$ and $3/4$ resonances are shown for prograde and retrograde orbits with $e = 0.6$ around a Kerr black hole for several different spin values. We see that the typical shape of the resonances shown in Fig. 5 is preserved. Prograde resonances with larger spin values are closer to the black hole in comparison to the point $p^*$ whereas retrograde resonances associated with higher spin values occur further outward. The shapes of these resonances are in qualitative agreement with the weak field *U-I* transition discussed with respect to Fig. 3.

A quantitative comparison between the numerically computed position for the 2/3, 6/7, 14/15 and 29/30 resonances and the weak field approximation developed in Sec. V B is given in Fig. 7. The analytic result is obtained from Eq. (32), with $e = 0.6$ and varying spin values. The weak field approximation provides a good fit for high orbital inclination ($z_-^2 = 1$) even when $p < 20$. The weak field approximation deviates more strongly from the analytic results as the spin value increases, such that the orbits with $a = 0.2$ exhibit a better fit than those for which $a = 0.99$. For a given spin value the approximation fits the retrograde orbits (higher $p$) better than the corresponding prograde orbits (lower $p$). This is to be expected since in the approximation of Sec. V B we used a quadratic approximation to the resonance condition valid only for $p \to \infty$ and included spin effects only up to $O(a^2/p^2)$. Figure 7 also shows the analytic solution on the equatorial plane as calculated from the roots of Eq. (41) with the added second-order correction for nonzero eccentricity $p^* e^2/4(p^* - 6)$ given in Eq. (49). These equatorial solutions are in very good agreement with the numerical results. They provide an easily computed indicator of where the weak field approximation strongly departs from the analytically computed surfaces.

## VI. THE LOCATION OF RESONANT SURFACES IN TERMS OF $E$, $L_z$ PARAMETERS

When conducting numerical investigations of orbits in spacetimes that are more general than Kerr it is often useful to plot a Poincaré map at fixed $E$ and $L_z$ as a diagnostic tool to explore the breakdown of KAM tori. This method of surveying the parameter space is not as well suited for describing the physical location of the orbit, but it unambiguously generalizes to metrics where a Carter constant $Q$ does not exist. In this section we develop some intuition for the features of resonant surfaces in $E$, $L_z$ space. This picture will be invaluable as we discuss departures from integrability and torus breakdown in the next section.

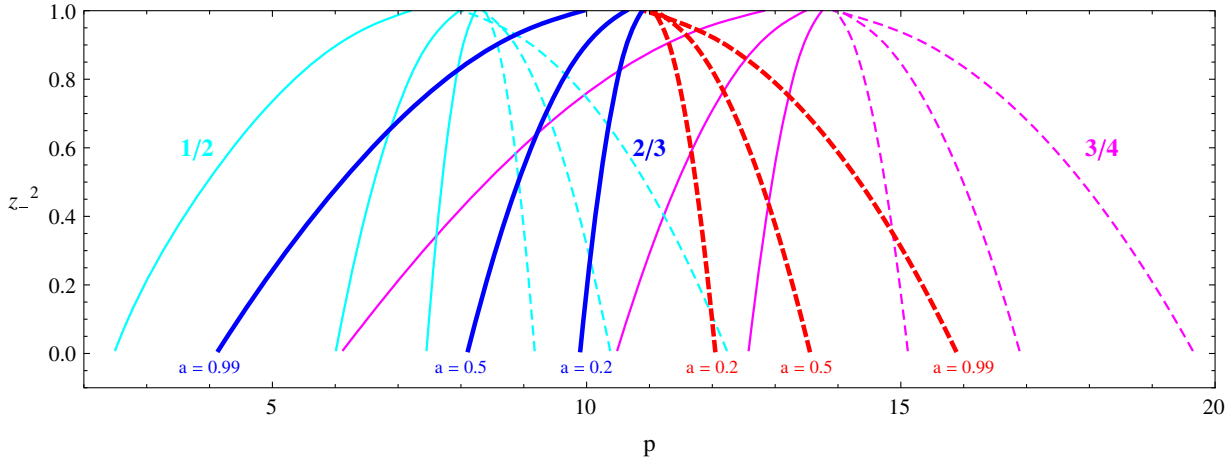


FIG. 6 (color online). The numerically computed location of the $1/2$, $2/3$ and $3/4$ resonance for fixed eccentricity $e = 0.6$ for the spin values $a = 0.2, 0.5, 0.99$. (These are the same spin values used in Fig. 5.) The resonances for prograde orbits are shown in solid lines and those for retrograde orbits in dashed lines. The resonances appear centered around the corresponding $p^*$ values given in Table I, with the $1/2$ resonance (cyan) centered around $p^* = 8$, the $2/3$ resonance (blue and red) centered around $p^* = 10.8$ and the $3/4$ resonances (magenta) around $p^* = 13.7$. The features of these plots agree qualitatively with those of Fig. 3.

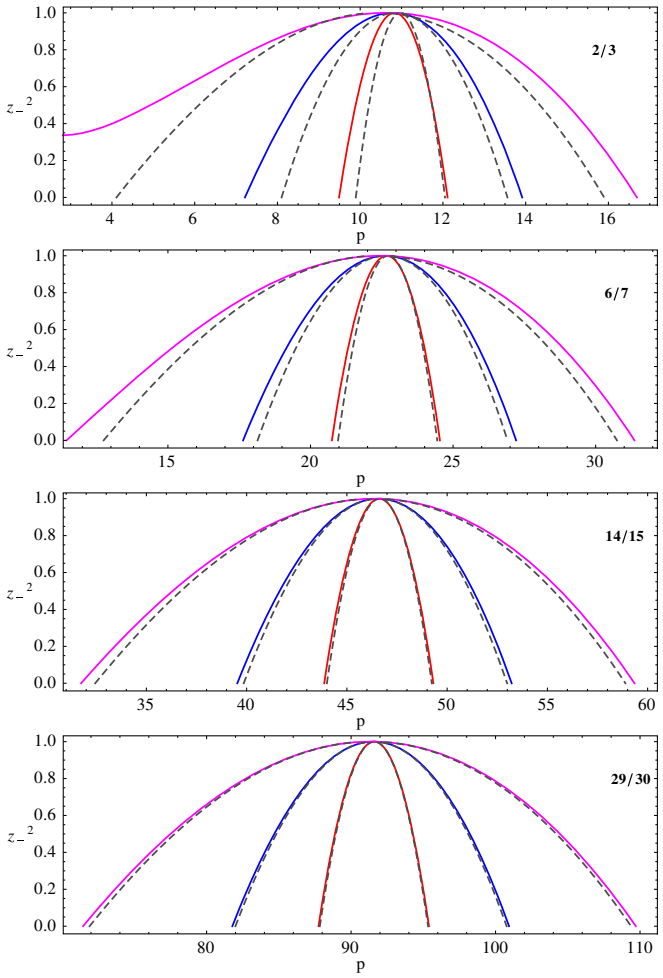


FIG. 7 (color online). Quantitative comparison between the numerically calculated resonance surfaces and weak field approximation of Sec. V B for the 2/3, 6/7, 14/15 and 29/30 resonances. The eccentricity is fixed at $e = 0.6$. The weak field approximation is computed using Eq. (32) and is shown for spin values $a = 0.2$ in red (inner arch), $a = 0.5$ in blue (middle arch) and $a = 0.99$ in magenta (the outer arch). The analytic results on the equatorial plane are shown in matching colored dots, with the numerical solutions overlayed using black dashes.

In Fig. 8 we show the 2/3 resonant surface for a maximally spinning black hole, $a = 1$, computed using the second numerical method of Sec. V E. In this figure the dots correspond to computed points on the resonance surface. The lines indicate fixed values of eccentricity and longitudinal angles at which the sampling took place: horizontal lines correspond to $z_-^2 = \{0, \sin(\pi/8), 1/\sqrt{2}, \cos(\pi/8), 1\}$, and the bent arches correspond to $e = \{0, 1/4, 1/2, 3/4, 1\}$. For each point $(p, e, z_-^2)$ on the resonant surface, the corresponding $E$ and $L_z$ values were computed using Eqs. (10) and (11). Care was taken to compute the appropriate $\varpi_\times$ root associated with the retrograde $p_-$ or prograde $p_+$ branch of the resonant surface under consideration. The outcome is shown in

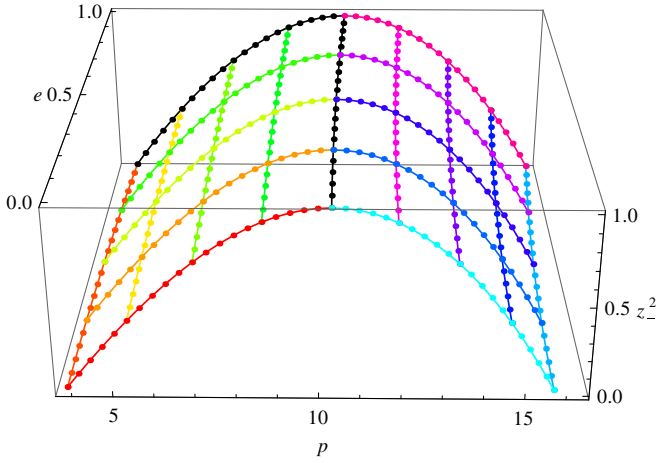


FIG. 8 (color online). The 2/3 resonant surface for a maximally spinning black hole $a = 1$ represented in terms of $(p, e, z_-^2)$ coordinates. Horizontal lines indicate longitudinal values of $z_-^2 = \{0, \sin\frac{\pi}{8}, 1/\sqrt{2}, \cos\frac{\pi}{8}, 1\}$; the bent arches indicate eccentricities of $e = \{0, \frac{1}{4}, \frac{1}{2}, \frac{3}{4}, 1\}$

Fig. 9. Note the large asymmetry about the $L_z = 0$ line that is due to the fact that the black hole is maximally spinning. The low energy spike that coincides with prograde orbits close to the equatorial plane with low eccentricity is easy to miss numerically when exploring the parameter space in terms of $E$, $L_z$ parameters. This spike constitutes a set of parameter values that potentially have important astrophysical implications: Most particles in thin astrophysical discs around rapidly spinning black holes are expected to be prograde and on nearly circular equatorial orbits. As the spin of the black hole decreases the resonance footprint on the $E$, $L_z$ plane will become increasingly symmetrical as is shown in Figs. 10 and 11.

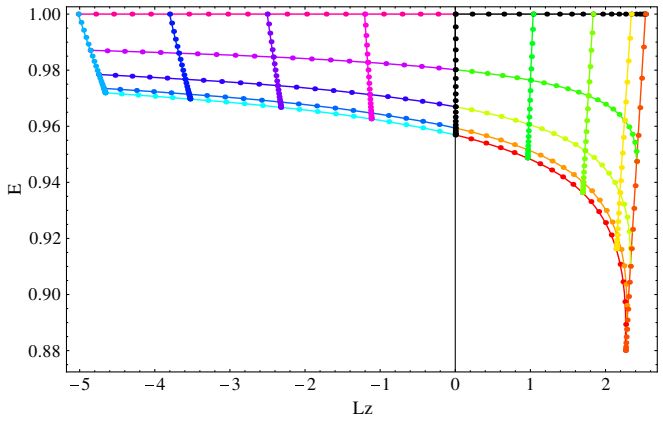


FIG. 9 (color online). The 2/3 resonant surface for $a = 1$, $\mu = 1$ projected onto $E$, $L_z$ coordinates [7]. Lines indicate constant values of $z_-^2 = \{0, \sin\frac{\pi}{8}, 1/\sqrt{2}, \cos\frac{\pi}{8}, 1\}$, and $e = \{0, \frac{1}{4}, \frac{1}{2}, \frac{3}{4}, 1\}$ corresponding to those in Fig. 8. The large asymmetry across the $L_z = 0$ line is indicative of the large spin value under consideration.

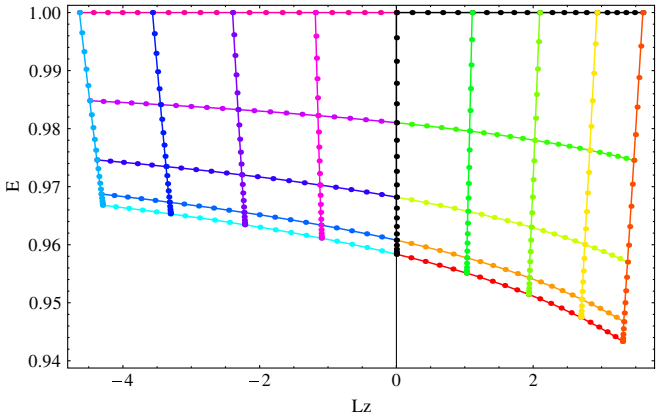


FIG. 10 (color online). The 2/3 resonance for $a = 0.5$ in $E$, $L_z$ coordinates for $z_-^2 = \{0, \sin\frac{\pi}{8}, 1/\sqrt{2}, \cos\frac{\pi}{8}, 1\}$, and $e = \{0, \frac{1}{4}, \frac{1}{2}, \frac{3}{4}, 1\}$, with units $\mu = M = 1$. Note the decrease in asymmetry across the $L_z = 0$ line when compared to Fig. 9 which is maximally spinning.

In Fig. 12 the $E$, $L_z$ projection of the 3/4 resonance surface is given for a black hole with spin $a = 0.5$. The higher-order resonance surface has features that are qualitatively similar to those of the 2/3 resonance of equal spin shown in Fig. 10. For the higher-order resonances however the $E$ values are slightly higher and the $L_z$ values span a marginally larger range.

From the figures in this section it should be clear that the representation of orbital parameters in terms of the $(p, e, z_-^2)$ coordinates is better adapted to the geometry of the resonant orbit, making it generally easier to quantify the resonance surfaces using these variables. Once obtained the resonant surfaces projected onto the $E$ and $L_z$ orbital variables can potentially be used to aid numerical exploration into Kerr-like spacetimes discussed in the next section.

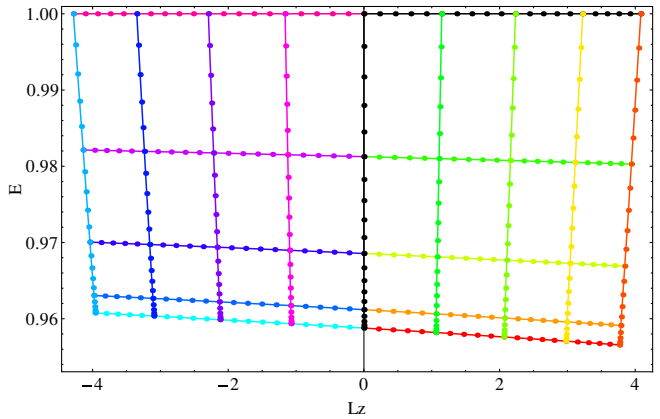


FIG. 11 (color online). The 2/3 resonance for $a = 0.1$ in $E$, $L_z$ coordinates for $z_-^2 = \{0, \sin\frac{\pi}{8}, 1/\sqrt{2}, \cos\frac{\pi}{8}, 1\}$, and $e = \{0, \frac{1}{4}, \frac{1}{2}, \frac{3}{4}, 1\}$. Since the spin is almost vanishing the figure is much more symmetrical about the $L_z$ axis than Figs. 10 and 9.

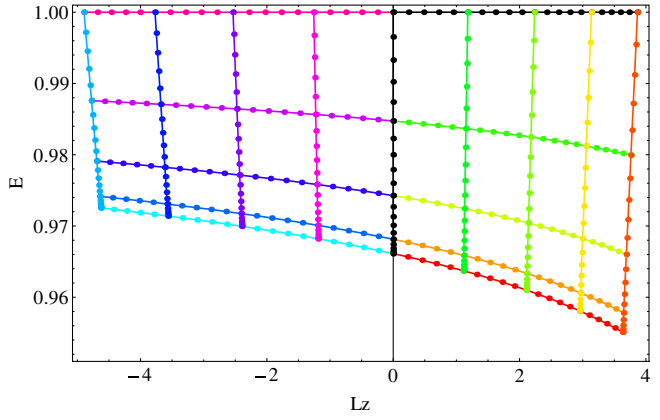


FIG. 12 (color online). The 3/4 resonant surface for $a = 0.5$ projected onto $E$, $L_z$ coordinates, for $z_-^2 = \{0, \sin\frac{\pi}{8}, 1/\sqrt{2}, \cos\frac{\pi}{8}, 1\}$, and $e = \{0, \frac{1}{4}, \frac{1}{2}, \frac{3}{4}, 1\}$. The main difference between the parameter space covered by the 2/3 and 3/4 resonance in Fig. 10 is that slightly lower energies are reached for the lower-order resonance and for the higher-order resonance the $L_z$ values have a marginally larger span; the other features remain qualitatively similar.

## VII. ROTATION CURVES AND THE BREAKDOWN OF KAM TORI

A number of groups have numerically explored the breakdown of integrability in stationary axisymmetric vacuum metrics such as the Manko-Novikov metric that reduces to the Kerr metric for a certain choice of parameters [13–15,17,58]. One of the tools used to explore the non-Kerr spacetimes numerically is to plot the Poincaré map of the orbital motion for a fixed choice of energy ($E$) and angular momentum ($L_z$). An example of a Poincaré map exhibiting broken tori is given in Fig. 13. Each closed curve

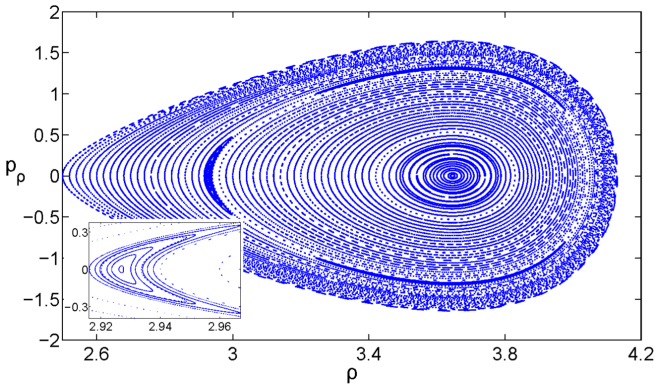


FIG. 13 (color online). A Poincaré map generated for the Manko-Novikov metric. The inlay shows a closeup of one of the islands in the Birkhoff chain of multiplicity 3. This island is associated with the breakdown of the 2/3 resonance as indicated using the rotation curve in Fig. 14. The spin value for this simulation was chosen to be $a = 0.9$ and the dimensionless quadrupole deviation parameter $q = 0.95$ was chosen to be very large. The other orbital parameters are $E = 0.95$, $L_z = 3$ and rest mass $\mu = 1$.

in the Poincaré map corresponds to an orbit that was started on the equatorial plane and given an initial momentum out of the plane. Each intersection of the orbit with the equatorial plane generates a point on the Poincaré map. The radial coordinate (here $\rho$) and corresponding radial momentum ($p_\rho$) of these piercing points are plotted. The closed curves in this Poincaré map indicate that for most initial conditions geodesic motion in the Manko-Novikov metric remains integrable or regular. However, among the closed curves, a Birkhoff chain of islands can be seen (enlarged in inset), which indicates that for certain initial conditions the regularity of orbits break down. This breaking of regular structure is associated with resonances in the fundamental frequencies describing the orbit as predicted by the KAM theorem.

The second diagnostic tool that gives insight during a numerical exploration is the rotation curve. This is a plot of the frequency ratio $\omega_r/\omega_\theta$ as a function of initial conditions for the Hamiltonian potential being studied. For an integrable system the rotation curve is a smooth function of initial conditions. In systems for which the KAM tori have broken, there are plateaus in the rotation curve where the numerically computed rotation number [59,60] remains roughly constant. This situation is depicted in Fig. 14.

In the numerical investigation of the Manko-Novikov metric, the breaking of low-order resonant tori is observed most dramatically at the $2/3$ resonance. The apparent dominance of the $2/3$ resonance over other integer ratios could heuristically be explained by the fact that in these studies, the deviation from Kerr was mainly a quadrupole perturbation and thus roughly proportional to $\cos 2\theta$. This geometric dependence of the perturbation indicates that any $2/m$ resonance is expected to be strongly excited. Integers other than $n = 2$ would arise from the nonlinear coupling between the angle variables and the coordinates, which is a higher-order effect. Since $\omega_r < \omega_\theta$ for Kerr we always have that $m > n$, so $2/3$ is the resonance with the lowest-order integer ratio. It is thus expected to dominate the breakdown of integrability for a system subjected to a quadrupole perturbation.

The numerical explorations of the breakdown of KAM tori has to date been limited to a very small subset of the allowed parameter space. To guide future studies covering the entire parameter space associated with the $2/3$ and $3/4$ resonances discussed in Sec. VI, we now describe how to use the machinery developed in this paper to analytically compute the rotation curve for the Kerr metric. An important caveat to bear in mind when exploring large deviations from the Kerr metric is that although the torus structure is not destroyed it may be distorted and the breakdown of quasiperiodic orbits may be shifted from the exact location of the resonance predicted by the rotation curve for orbits in Kerr spacetime. To zeroth order, however, the Kerr rotation curve provides an indication of the interesting regions in the parameter space.

For the Kerr metric the rotation curve is computed by evaluating Eq. (50) for a fixed $E$ and $L_z$ using the parameters defined in Eq. (25). A representative example is given in Fig. 15. For a given $E$ and $L_z$, bound orbital motion is usually restricted to a small region of physical space. Equatorial orbits ($Q = z_- = 0$) have the largest radial extent while circular orbits ($e = 0$) have the largest longitudinal reach, $z_{-\,\max} = z_-(e = 0)$. These two extreme points define the boundaries of the rotation curve. We examine them more closely by first computing the variables $\{p, e, z_-\}$ and subsequently the ratio $\omega_r/\omega_\theta$.

On the equatorial plane, $z_{-\mathrm{eq}} = 0$ and the radial potential Eq. (4) has one zero root; thus $\varpi_\times = 0$. The largest two roots of the remaining cubic determine $p_{\mathrm{eq}}$ and $e_{\mathrm{eq}}$. First

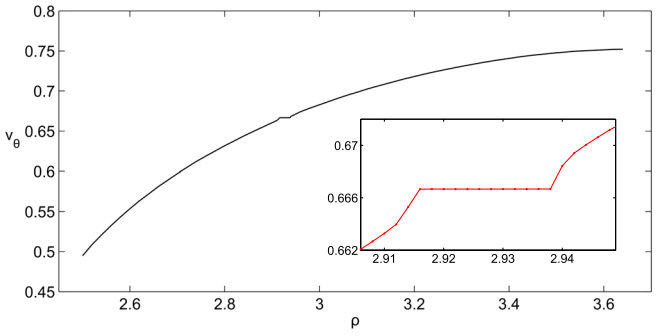


FIG. 14 (color online). The rotation curve is obtained by calculating the rotation number of each orbit from the Poincaré map given in Fig. 13. The rotation number, $\nu_\theta$, which is equal to the ratio of orbital frequencies, $\omega_r/\omega_\theta$, is plotted as a function of the initial radial coordinate of the orbit. The rotation curve is generally smooth and monotonically increasing. However, corresponding to the Birkhoff chains of islands seen in the Poincaré map, there is a plateau in the rotation curve for which $\omega_r/\omega_\theta = 2/3$ is resonant.

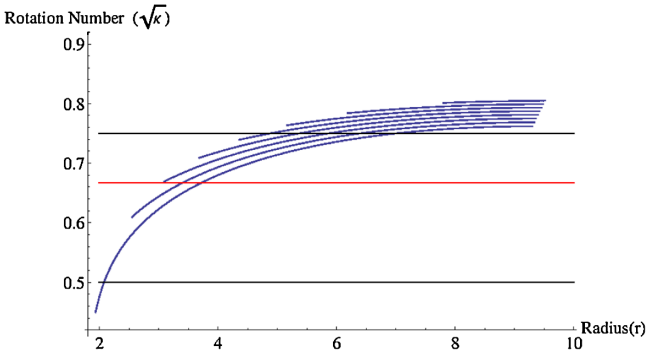


FIG. 15 (color online). The rotation curves for geodesics with $E = 0.95\mu$, in a Kerr black hole spacetime with spin $a = 9/10$. The different curves correspond to different $L_z$ values uniformly spaced between $L_z = 2.482\mu$ (lower curve) and $L_z = 3.343\mu$ (upper curve). For reference purposes, the $2/3$ resonance value is indicated by the central red line, the $1/2$ resonance by the lower black line and the $3/4$ resonance by the upper black line. The radius (r) refers to the radius of closest approach of the orbit to the black hole, i.e. its periastron $r_2$ given in Eq. (8).

consider the effect of eccentricity $e_{\rm eq}$ where the two extreme cases for bound orbits are $e_{\rm eq}=0$ and $e_{\rm eq}=1$. Making use of Eq. (40) we have that if $e_{\rm eq}=0$ the rotation curve reduces to a single dot at

$$\omega_r/\omega_\theta=\sqrt{\frac{(p-6)p-3a^2\pm 8a\sqrt{p}}{p^2+3a^2\mp 4a\sqrt{p}}}. \tag{51}$$

If the $E$ and $L_z$ values have been chosen to lie on the $2/3$ resonance, this value would correspond to either the lower rightmost or lower leftmost points in Figs. 9, 10 and 11 depending on the spin of the black hole and whether the retrograde (left) or prograde (right) orbit is under consideration. Equation (51) in conjunction with Eqs. (36) and (38) can be used to estimate the characteristic $E$ and $L_z$ associated with the $\kappa$ resonance in the nonspinning limit to be

$$\frac{E^2}{\mu^2}=\frac{2(2+\kappa)^2}{9(1+\kappa)},\qquad \frac{L_z^2}{\mu^2}=\frac{12}{1-\kappa}. \tag{52}$$

For the $2/3$ resonance this evaluates to $E=0.95879\mu$ and $L_z=\pm 3.86702\mu$. If the spin is maximal, $a=1$, the prograde branch has $E=0.88009\mu$, $L_z=2.26471\mu$, $p=3.86704$ while the retrograde branch has $E=0.971899\mu$, $L_z=-4.6614\mu$, $p=15.733$. These values can be compared to the lower corner points in Fig. 9.

For parabolic equatorial orbits, $e_{\rm eq}\to 1$ and $E=\mu$. This case corresponds to the largest possible radial extent a marginally bound orbit can have. For the $2/3$ resonance these values are indicated by the upper leftmost and upper rightmost points on Figs. 9, 10 and 11. We define the dimensionless angular momentum parameter $l_z=L_z/\mu$ and note that on the equatorial plane, $\varpi_\times=0$, $\varpi_+=l_z/2$. Using Eqs. (10) and (11) implies that the values of $p$ are restricted to

$$p=\frac{l_z^2}{2}\left(1\pm\sqrt{\left(1-\frac{4}{l_z}+\frac{4a}{l_z^2}\right)\left(1+\frac{4}{l_z}-\frac{4a}{l_z^2}\right)}\right). \tag{53}$$

The factor under the square root is positive only if $l_z>2(1+\sqrt{1-a})$ or $l_z<-2(1+\sqrt{1+a})$. The smallest value of $p$ that can be attained for equatorial parabolic orbits is thus $p_\pm=2(1+\sqrt{1\mp a})^2$ for prograde ($p_+$) and retrograde ($p_-$) orbits respectively.

The parameters that enter into Eq. (24) for equatorial parabolic orbits are

$$\frac{y_1}{y_2}=\frac{3p-l_z^2}{2l_z^2},\qquad \frac{\delta_1}{y_1}=\frac{l_z^2-p}{l_z^2-3p},\qquad \frac{\delta_2}{y_2}=0. \tag{54}$$

Evaluating Eq. (50) we find that $\sqrt{\kappa}$ is a monotonically increasing function of $p$ or equivalently $l_z$. In the limit of a spin zero black hole the resonance $\sqrt{\kappa}=2/3$ occurs when $p=11.3273$, $l_z=4.18461$. Parabolic orbits with larger $|l_z|$ will not sample the $2/3$ resonance regardless of inclination. For a maximally spinning black hole, the $2/3$ resonance occurs at $p_-=16.2914$, $l_z=-5.01845$ for retrograde orbits and at $p_+=4.14634$, $l_z=2.53177$ for prograde orbits (see Fig. 9).

Finally we consider the maximal vertical extent an orbit can have. This occurs for circular orbits given a fixed $E$ and $L_z$. If $e=0$, $\delta_1/y_1=0$ and $\varpi_+=-2p+\frac{2}{1-E^2/\mu^2}$. Equation (11) gives $\varpi_\times$ to be

$$\varpi_\times=\frac{a^2(1-2\frac{E^2}{\mu^2})+2a\frac{E}{\mu}l_z+p(\frac{E^2}{\mu^2}(p-3)p-(p-2)^2)}{(p-1)(\frac{E^2}{\mu^2}-1)}, \tag{55}$$

which can be substituted back into $L_z^2$ in Eq. (10) to give a polynomial in $p$ that can be solved to find $p_{e=0}$ for the given $E$ and $L_z$. Substituting these results into the remaining expansion parameters of Eq. (25) and evaluating Eq. (50) yields the maximum value the rotation curve attains.

## VIII. ESTIMATING THE SIZE OF THE PERTURBATION THAT RESULTS IN A DRAMATIC CHANGE OF DYNAMICS DUE TO TORUS BREAKDOWN

The KAM criterion for the possible destruction of tori can be augmented by further estimates. A generic analytic perturbation $F(r,\theta,p_r,p_\theta,p_\phi)$ to geodesic quantities such as the energy can be written as a Fourier expansion of the form

$$F(r,\theta,p_r,p_\theta,p_\phi)=\sum_{\mathbf{n}=-\infty}^{\infty}F_{\mathbf{n}}(e,p,z_-)e^{i\mathbf{n}\cdot\mathbf{q}}, \tag{56}$$

where $\mathbf{q}$ are the angle variables corresponding to the frequencies via

$$\frac{d\mathbf{q}}{d\lambda}=\omega+O(\epsilon). \tag{57}$$

For most orbits, all the Fourier components in Eq. (56) with $\mathbf{n}\neq 0$ will be oscillatory and their contribution approximately averages out over an orbit. The orbit's leading-order secular evolution is driven by the component with $\mathbf{n}=0$. However, at a resonance where $\mathbf{k}\cdot\omega=0$ the Fourier components in Eq. (56) that involve the resonant combination $(\mathbf{k}\cdot\mathbf{q})$ momentarily cease to be oscillatory since their phase becomes stationary. These components thus generically contribute order unity corrections to the secular evolution over the resonance time, except when the amplitude of these components is $O(\epsilon)$ or smaller. Since for analytic functions the Fourier amplitudes $F_{\mathbf{k}}$ fall off

exponentially with $\mathbf{k}$, we expect the resonance to have an appreciable effect on the dynamics only when

$$O_{\mathbf{k}} = \sum_i |k_i| \lesssim O(|\ln(\epsilon)|). \tag{58}$$

This criterion on $\mathbf{k}$ in (58) for "essential" resonances [61] refines the bound for sufficient irrationality discussed in Eq. (2) for the special case of analytic perturbations.

For EMRIs with the only source of perturbation being the gravitational self-force, even the low-order resonances are expected to be weak in the sense that the dominant dissipation $F_{\mathbf{0}}$ is generically larger than the resonance potential related to $F_{\mathbf{k}}$. The resonances will therefore appreciably modify but not destroy the object's continued inspiral. Now, however, consider the case of additional perturbations that lead to very strong resonance modifications, where heuristically $F_{\mathbf{k}} \gg F_{\mathbf{0}}$. Chirikov's resonance overlap criterion [62] specifies the conditions under which the complete loss of quasiperiodic motion is expected to occur as follows. Each strong resonance captures orbits in its vicinity and is thus surrounded by an oscillation region similar to the Birkhoff islands shown in Fig. 13 and manifests as a plateau in the frequency evolution similar to that in Fig. 14. The onset of full-blown chaos occurs when these Birkhoff chains associated with nearby resonances become large enough that they touch. More precisely, Chirikov's criterion states that the transition to stochastic behavior arises when two neighboring strong resonances overlap in the sense that the frequency width of their oscillation regions is larger than their spacing in frequency. An estimate for the width of the resonance regions is [62,63]

$$\Delta|\mathbf{k}\cdot\omega| \sim \sqrt{\epsilon}\sqrt{|(\mathbf{k}\cdot\omega)_{,J_\alpha} F_{\alpha\mathbf{k}}|}, \tag{59}$$

where $J_\alpha = (e, p, z_-)$ and $F_{\alpha\mathbf{k}}$ are the forces such that $\dot{J}_\alpha = \epsilon F_\alpha + O(\epsilon^2)$ and $F_\alpha$ is Fourier expanded as explained above. Overlap occurs for two resonances associated with lattice vectors $\mathbf{k}$ and $\mathbf{k}'$ respectively when

$$\Delta\omega_i^{(\mathbf{k})} + \Delta\omega_i^{(\mathbf{k}')} > |\omega_i^{\mathbf{k}} - \omega_i^{\mathbf{k}'}| \tag{60}$$

for each of the frequencies $\omega_i$ evaluated at the resonances of the unperturbed system. This estimate of the criterion for overlap is only a crude indicator for the transition to stochasticity, and in cases of interest the local dynamics must be systematically analyzed [64,65].

For most systems explored numerically to date, the plateaus in the rotation number curve remain small, and thus do not satisfy Chirikov's criterion. This indicates that we expect at most weak chaos in the sense that torus disruption, if it occurs, is limited to a small region in phase space.

## IX. ASTROPHYSICAL IMPLICATIONS

For astrophysical processes near supermassive black holes the Kerr geometry usually provides the background stage on which several small perturbation effects play their part. In select regions of the spacetime corresponding to low-order resonant orbits the smooth distortion due to perturbation induced effects is disrupted. The background spacetime geometry largely sets the location of these resonance induced disruptions imprinted on the dynamical structures of the perturbed system, while their details depend on the properties of the perturbations.

Generally these effects are expected to be small, although persistent and robust. They are induced by all nonintegrable perturbations of the Kerr metric. If the perturbation is not too large resonant effects occur at the locations quantified in this paper irrespective of the source of the perturbation. Table I indicates the characteristic length and time scales associated with resonances in dimensionless units and as well as in units characteristic of the region around Sgr A*. In Fig. 16 we have plotted all the low-order resonances with order $O_\kappa = n + m \leq 15$ superimposed on an embedding diagram for a nonspinning black hole. This plot gives an indication of how strongly the spacetime for a particular resonant surface is curved and the relative extent of the regions of influence of the low-order resonances. Note the accumulation of resonances near the ISO which can also be observed in Fig. 4 and persists for the spinning case. In Fig. 16 we have scaled the width of the

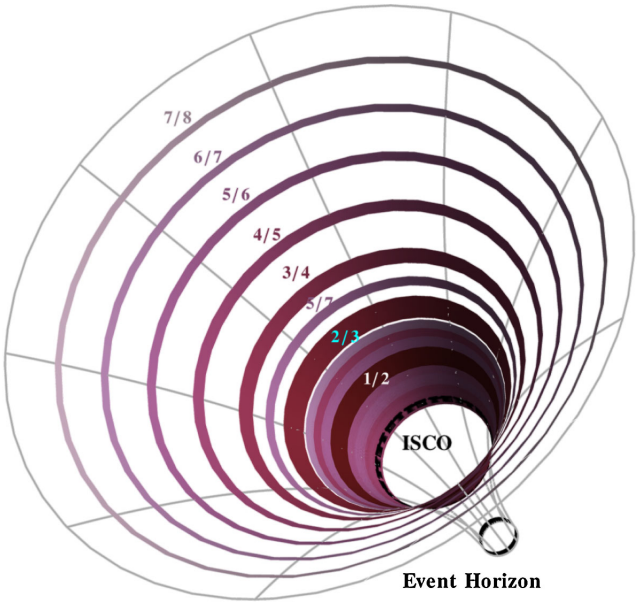


FIG. 16 (color online). The location of low-order resonances around a black hole [7]. Here low-order resonances are plotted superimposed on an embedding diagram to give an indication of how strongly the spacetime in their vicinity is curved. The line width in each case is scaled with $3/O_\kappa$ where $O_\kappa = m + n$ to give an indication of the relative importance of a particular radius. This image gives an overestimate of the importance of higher-order resonances since the correct scaling according to Eq. (2) is $K/O_\kappa^3$.

lines demarcating each resonance by $K(\epsilon)/O_\kappa$ with an arbitrary choice of $K = 3$ to result in good rendering. Recall that Arnold's criterion, in Eq. (2), governs the persistence of tori scales as $K/O_\kappa^3$. Higher-order resonances are thus likely to be strongly suppressed compared to the schematic representation given here.

The three lowest-order resonant tori, $1/2, 1/3, 2/3$, whose parameters are indicated in bold in Table I are mathematically most likely to break. Of these it is likely that astrophysically the $2/3$ resonance will have the greatest probability of being directly observable based on the following arguments: (i) For an EMRI, the impact of the broken resonance is likely to be larger if the perturbing object remains in the vicinity of the resonance for a considerable amount of time. The $1/2$ and $1/3$ resonances lie at $4R_S$ and $3.4R_S$ respectively, close to the ISO at $3R_S$ where the radiation reaction force is large and the orbit is transitioning to the plunge phase. The time and number of orbits that an inspiraling object of mass $\mu$ spends near a given radius roughly scale as $t \sim p^4/(\mu/M)$ and $N \sim p^{5/2}/(\mu/M)$; thus the influence of the $2/3$ resonance can accumulate longer than for the $1/2$ and $1/3$ resonances. See also Ref. [9] for more precise estimates. (ii) For electromagnetic observations, the fact that the $1/2$ and $1/3$ resonances lie in the region of high curvature and possibly near or on the edge of the accretion disc is likely to confuse any distinct signal originating from this region. The $2/3$ resonance on the other hand is located at roughly $5.4R_S$ further out of the potential well, making it easier for electromagnetic radiation to escape. (iii) The final reason for expecting the $2/3$ resonance to dominate is akin to the discussion in Sec. VII where it was argued that quadrupolar gravitational potential perturbations will preferentially excite the $2/3$ rather than lower-order resonances.

If the resonance condition is satisfied the particle motion either passes through the resonance, or, when the resonance dominates over dissipation so that $F_{\mathbf{k}} > F_{\mathbf{0}}$ in Eq. (56) holds and depending on the initial conditions, the object can temporarily be captured in the resonance. For captured particles the resonance effectively fixes the orbital frequency ratio of the object's orbit which manifests as a plateau in its rotation curve, as seen in Fig. 14. This is indicative of a stable, attracting resonance. Repelling resonances, typified by an inflection point or jump in the rotation curve, are associated with unstable periodic orbits [59,66] and will be short lived in the presence of dissipative effects. The detailed study of the dynamics when a small mass enters the resonance region under various forms of perturbation is the subject of future work and has been studied in a particular Newtonian case in [67]. In the event of resonant capture the orbital parameters will linger within the resonance surface, possibly altering constants of motion because of the interchange of energy and angular momentum between the perturbation and the orbit. When the gravitational radiation reaction is significant, the dissipation will most likely cause the orbit to evolve towards a lower energy state, i.e. increasingly circular equatorial configurations, corresponding to the lower right-hand corner of Figs. 8 and 9.

Now consider a collection of particles in a low-density accretion disk around an astrophysical black hole. As explained in the Introduction, their orbits will be influenced by a number of small perturbations which could cause them to become captured by a resonance, since the gravitational dissipation is small for low mass ratios. The evolution towards prograde circular equatorial orbits during resonance will limit the collisional interaction of the swarm of trapped particles, potentially creating a cohesive structure. It is thus possible that the characteristic structure associated with the resonances, such as the resonance zones visualized in Fig. 16, will be imprinted on any thin disk surrounding a black hole in the form of density inhomogeneities in much the same way as the resonant structures imprinted on Saturn's rings [4]. Unlike the rings of Saturn where matter largely remains captured indefinitely, the black hole rings will be dynamical because radiation reaction will alter the resonant structures and enable escape from resonance (as can be quantified using e.g. the methods in [68]). In this scenario, when a trapped overdensity becomes massive enough for the radiation reaction force to become important the black hole ring will partially disintegrate, depositing an overdensity of matter on the next inward ring in the disk. There, the matter will again be trapped for some time before continuing the infall. Thus in one related catastrophic event the whole ring structure will readjust, with the emitted radiation carrying an imprint of the particular resonances involved. Provided the accretion rate is slow enough the ring structure will reform after each radiation reaction dominated ring collapse event. Since the radiation reaction force scales with mass ratio it is further expected that there will be a segregation in the particle sizes found in each ring. The tendency for captured orbits to evolve to a more circular, equatorial configuration is expected to minimize the ejection of simultaneously captured particles due to collisional interactions.

Another mechanism that could excite the resonant ring structure and lead to a distinct signature in the emitted radiation is the collision of a compact object with the matter in successive rings. The resulting collisional hot spot of excited gas will rotate with an azimuthal frequency set by the characteristic resonance surface. A detailed study of the possibility of a ring structure, its dynamics and observational signatures is left for future work.

We now conduct a very precursory search for phenomena that could possibly be associated with the resonant structure around black holes. The closest supermassive black hole at the center of our Galaxy presents an interesting test bed. Recent monitoring of Sgr A* with the 1.3 mm very-long-baseline interferometry showed time-variable structures on scales of $\sim 4R_s$ [69,70]. The physical origin of this structure is not yet clear, but it is interesting to note that the scale is similar to that of the low-order resonances given in Table I. As discussed above it is

possible that temporary capture of material or gas near the resonance location could lead to a time-varying signature in the photon emission. For argument's sake, suppose that the origin of the structure at $\sim 4R_S = 8M$ is in fact the $2/3$ resonance but displaced from the nonspinning value listed in Table I because Sgr A* has spin. Using Eq. (45) the spin displacement of the prograde $2/3$ resonant surface is $p_+ = 10.8 - 5.36a$. From the amount of spin displacement of the resonance needed to match the observed structure one could then infer that Sgr A* has $a = 0.5$. The plausibility of identifying this structure with the $2/3$ resonance could be confirmed if the variability has characteristic time scales of slightly less than an hour. The increase in sensitivity of the very-long-baseline interferometry measurements will enable resolving more of the horizon scales, and it will be fascinating to see if the resonance structure can be revealed. Table I provides a quick reference for the possible characteristic time and length scales. Note that because the coefficients in Eq. (45) differ for different resonances, observing more than one resonant structure places an independent check on the veracity of this method of determining the spin, since the displacement of both resonances due to spin must be consistent.

Another example of a phenomenon that could potentially be associated with the orbital resonances is the quasiperiodic oscillations (QPOs) observed in the x-ray spectra of several black hole candidates. Four stellar mass black hole systems exhibit quasiperiodic variability with peaks at harmonic pairs of frequencies in a $2/3$ ratio; one also shows an additional $3/5$ ratio [71]. Recently, QPOs have also been identified in a supermassive black hole [72] and in a tidal disruption event [73]. A definitive physical explanation for the origin of the QPOs is currently lacking. Numerous models have been proposed, including orbital resonances of any combination of the three orbital frequencies and their corresponding beats [31,74], accretion disk oscillations with nonlinear effects [75–77], or variations in the geometry of the accretion flow [78]. For the case where both the $2/3$ and $3/5$ ratios are observed, it is very interesting to note from Table I that these two resonances are in fact nearest neighbors in $p$, with the $3/5$ occurring at just slightly smaller $p$ values than the $2/3$ resonance. A disruption event at the $2/3$ resonance could excite an event at the $3/5$ resonance because of their physical proximity. Measuring the frequencies of the observed resonances in QPO's will give further clues as to whether they can correctly be attributed to orbital resonances around Kerr or whether other physics dominate over the orbital dynamics.

The concentration of low-order resonances near the black hole and their absence further out has important implications for the key science objective of testing the no-hair theorems using a supermassive black hole such as Sgr A*. The no-hair theorems state that, provided the cosmic censorship and causality axioms hold, if the black hole's mass and spin are known the quadrupole moment is fixed. Liu *et al.* [79] have shown that recording the time of arrival signals of a pulsar orbiting Sgr A*, with orbital period $\sim 4$ months, for several years with the Square Kilometer Array (SKA) will enable us to measure the mass of Sgr A* to a precision of $10^{-6}$, the spin $10^{-3}$ and the quadrupole moment to $10^{-2}$. This will allow a definitive test of the no-hair theorems. The detection of a pulsar even closer to the central object could allow the extraction of additional multipole moments through long term monitoring, thus mapping out more and more details of the structure of the central black hole.

The analysis in this paper assures us that orbits around Sgr A* with a period of the order of weeks to months are sufficiently far from the low-order resonances that the KAM theorem guarantees quasiperiodic motion and the persistence of invariant tori under perturbations. This result implies that frequency drifts computed using perturbative methods based on averaging, as done in [80], accurately describe the physical system that is effectively free of stochastic motion. It also ensures that tracking the regular motion of a pulsar will reflect a map of the gravitational potential it samples. We conclude this section by mentioning in passing the relevance to future gravitational wave detectors such as eLISA and their potential to directly probe resonant dynamics. A detector sensitive to the frequency band $\sim 10^{-4}$–$10^{-1}$ Hz, observing an EMRI near SgrA* $M_{\mathrm{SgrA*}} \approx 4 \times 10^6 M_\odot$ [81], can probe mean radial distances ranging from the event horizon to $\sim 50M$ [17]. This overlaps with the region where the strongest resonances occur (see Table I ). The potential direct detection of gravitational wave emission from a resonance transit is an exciting possibility. It does however underscore the necessity to carefully model and incorporate resonant effects in the search templates. The loss of phase coherence as the small mass object passes through a resonance could potentially make parameter estimation difficult.

## X. SUMMARY AND DISCUSSION

In this paper we have computed the location and associated time scales of resonant orbits in the Kerr spacetime and commented on the observational and mathematical implications. We have considered resonances between the two fundamental frequencies corresponding to the radial and longitudinal motion, which are the key quantities relevant to phenomena associated with the underlying phase space of the system. Our results provide a complete survey of the parameter space of resonant orbits, together with simple expressions for locating the resonances valid in the strong field region. If resonant phenomena are observed these expressions could provide an easy way of determining the spin of the central black hole. We considered several examples of electromagnetic observations at different wavelengths that could be related to the capture and escape of material from resonances.

We have computed the resonant surfaces both in terms of generalized Keplerian variables (related to the orbital geometry) and projected onto the $E$ and $L_z$ parameter space (related to the spacetime symmetries) to help identify promising choices of parameters for numerical investigations of torus breakdown in resonance regions. We have further found an analytic expression for the rotation curve associated with the Kerr metric as a function of $E$ and $L_z$ that can be used for comparing to numerically computed rotation curves associated with Poincaré maps. We expect low-order resonances such as the $2/3$ and $1/2$ resonances to have the strongest observable effects on orbital motion, electromagnetic emission and the phase of emitted gravitational waves. These resonances occur in the strong field regions of the spacetime at a distance of $\lesssim 5.4R_s$ from the black hole and are fairly widely spaced by $\sim 1.4R_s$ in the limiting case of a nonspinning black hole.

According to the KAM theorem low-order resonances indicate where in a dynamical system the transition to chaos is likely to occur first. Such a transition requires a sufficiently large perturbation that could arise from various sources such as the non-Kerr nature of the spacetime, the internal structure of the probe, alternative theories of gravity or the presence of other bodies or gas. We summarized the KAM estimate and additional arguments by Arnold and Chirikov to assess which resonant tori are expected to survive under the perturbation and where dramatic changes in the dynamics could occur. Combining these general bounds with our results for the resonances indicates that there is a large region for mean radii $50R_s \lesssim p \lesssim 1000R_s$ where resonance effects are negligible but where the spacetime curvature is sufficiently high that multipoles of the central object have an observable effect on the motion. This will enable tests of the no-hair theorem unimpeded by drastic changes in the dynamics.

More stringent bounds than discussed in this paper on the occurrence of strong resonances and the transition to stochastic behavior require detailed studies of the dynamics near resonant tori for the different kinds of perturbations. We noted in Sec. VIII that for EMRIs the gravitational radiation reaction force, which is important in the region where low-order resonances occur, sets an approximate scale for the strength of the perturbation required to destroy the tori. In future work we intend to study the details of the breakup of the tori and quantify the strength of the perturbation required for observable consequences in each case.

Regions where lower-order resonances occur also earmark the most likely positions in phase space where averaging methods must be modified to account for the resonances. If an orbit passes through a resonance it effectively acquires a sudden change in the frequencies whose magnitude depends on the initial conditions. For sufficiently strong resonances, orbits can enter a resonance region, linger near it and subsequently escape. This manifests as a plateau in the frequency evolution similar to that seen in the rotation curve of Fig. 14 but tilted because of radiation reaction. More work will be needed to determine how well the frequencies must be resolved to detect such a plateau and exploit the measurements to determine the system parameters with LISA.

In addition to exploring the parameter space of resonances in this paper, we characterize in the Appendixes the locations of the innermost stable orbit beyond which geodesics plunge into the black hole. This provides a useful benchmark for the resonance locations and also indicates the region where zoom-whirl behavior would occur and where higher-order resonances accumulate.

## ACKNOWLEDGMENTS

This work was supported in part by National Science Foundation Grants No. PHY-0903631 and No. PHY-1208881, the Maryland Center for Fundamental Physics, the Square Kilometer Array project in South Africa and the National Institute of Theoretical Physics in South Africa.

## APPENDIX A: LOCATION OF THE INNERMOST STABLE ORBIT

In this appendix we explore the location of the ISO using the notation and variables given in Sec. III B. Observationally this is an important location in the black hole spacetime since it demarcates the radius from which the test mass will enter the plunge phase of its orbit. Near the ISO a noncircular orbit exhibits zoom-whirl behavior as the radial frequency goes to zero while $\omega_\theta$ and $\omega_\phi$ remain finite. The test mass will linger near its periastron for many periods of the $\phi$ and $\theta$ motion, then rapidly zoom out to apastron and back, giving rise to a characteristic signature in the emitted gravitational waves. When tracking the frequency evolution of a particular orbit, this determines the final set of $\omega_\phi$, $\omega_\theta$ frequencies that will be recorded before the test mass begins its plunge into the black hole. When discussing resonant orbits of a spinning black hole it is often useful to view their location relative to the location of the ISO for the same spin, inclination and eccentricity. The ISO surface (where $\omega_r$ vanishes) shares many of the qualitative features of the resonance surfaces (where the combination of frequencies $m\omega_r - n\omega_\theta$ vanishes) discussed in the main body of the text and both are related to degenerate structures in the phase space that are broken under small perturbations.

The ISO occurs when the potential barrier in the radial potential no longer shields the orbit from the singularity. Mathematically the condition that defines this orbit is that the middle two roots of Eq. (4) coincide,

$$r_3 = r_2 = \frac{p}{1+e}. \tag{A1}$$

This allows us to express the $\varpi_+$ and $\varpi_\times$ variables as

$$\varpi_+ = r_4 + \frac{p}{1+e}, \qquad \varpi_\times = \frac{r_4 p}{1+e}. \tag{A2}$$

Equation (14) allows us to find an expression for $z_-^2$ in terms of $r_4$,

$$z_-^2 = \frac{p(\tilde{r}_4(e-3)-(e+3)p)}{2a^2(e-1)(e+1)^2} + \frac{p\sqrt{(e-3)^2\tilde{r}_4^2+2(e^2+7)p\tilde{r}_4+(e+3)^2p^2}}{2a^2(e-1)(e+1)^2}, \tag{A3}$$

where we have set $\tilde{r}_4 = (1+e)r_4$ to yield a more compact expression. Equation (12) provides a quadratic equation for $r_4$ that allows us to determine its value in terms of $p$ and $e$. The solution can be written down in the form,

$$r_4 = (-B_{r_4} + \sqrt{\Delta_{r_4}})/A_{r_4}, \tag{A4}$$

with

$$\begin{aligned}
\Delta_{r_4} &= 64(e+1)p^3[p-(e-1)(\tilde{a}-1)][p+(e-1)(\tilde{a}+1)][p-(e+1)(\tilde{a}+1)]^2[p+(e+1)(\tilde{a}-1)]^2,\\
A_{r_4} &= a^4(e-1)^2(e+1)^4 - 4a^2(1-e)(3-e)(e+1)^3p + 2(e+1)^2p^2(a^2(3+e)(e-1)+2(e-3)^2)\\
&\quad - 4(e^2+7)(e+1)p^3 + (e+3)^2p^4,\\
B_{r_4} &= a^4(e-3)(e-1)(e+1)^3p - 4a^2(e+1)^2(e^2-2e+3)p^2 + 2(e+1)p^3(a^2(e^2-5)+2e^2+14)\\
&\quad - 4(e^2+2e+3)p^4 + (e+3)p^5.
\end{aligned} \tag{A5}$$

We have set $\tilde{a} = \sqrt{1-a^2}$. In Eq. (A4) we chose the "+" root of the quadratic to yield the correct behavior for $z_-^2$. The ISO surface exhibits many of the characteristics seen in the resonance surfaces studied in Sec. V. These include the fact that as inclination increases the $p$ values of the prograde/retrograde ISOs respectively increase/decrease until the two branches coincide for $z_-^2 = 1$. This behavior is due to the fact that polar orbits are less influenced by the spin of the black hole. Also note that for $z_-^2 = 1$, $dz_-^2/dp = 0$. A graphical representation of the ISO surface is given in Fig. 17.

We now give a number of easily evaluated formulas for special parameter values. For circular orbits around a

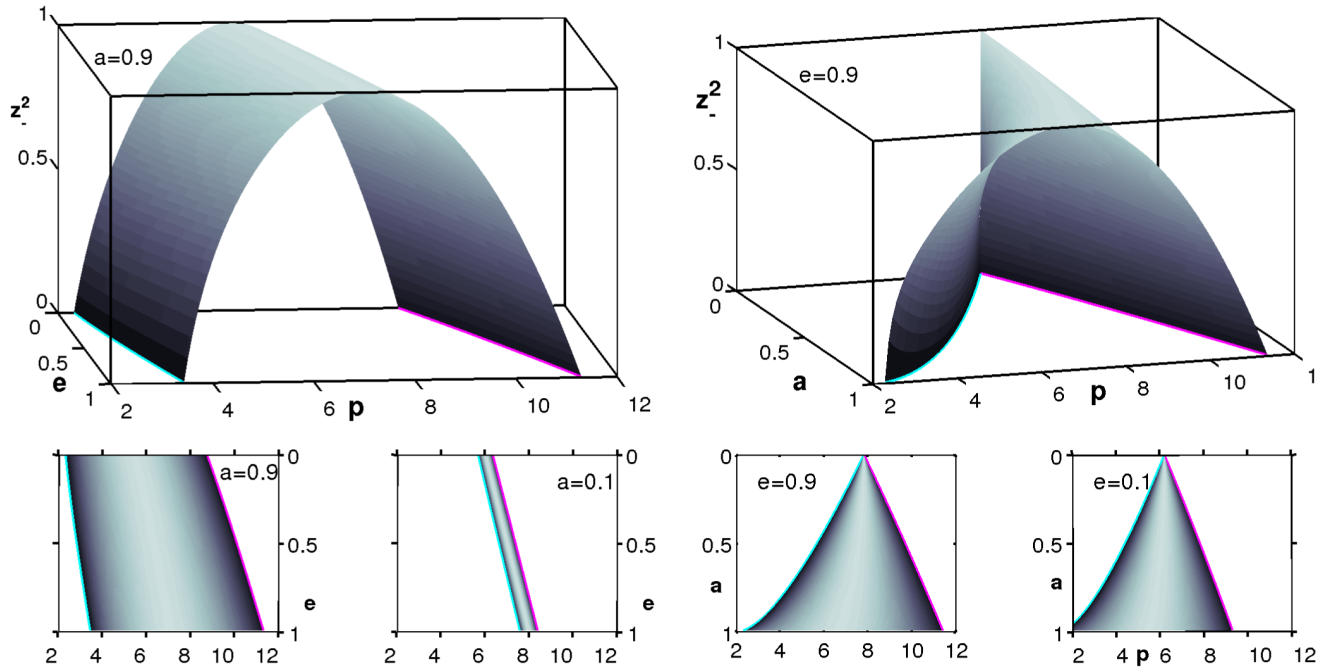


FIG. 17 (color online). Graphical representation of ISO surface constructed using Eqs. (A3)–(A4). The ISO surfaces displayed in the top two images show the same qualitative *U-V-I* transitions as the resonant orbits. Smaller images in the bottom row give the top view of the resonant surfaces for various spins and eccentricities. The top left and the two images on the bottom left display the eccentricity dependence for different spin values. The ISO is linearly dependent on eccentricity (as opposed to the quadratic dependence observed in resonant surfaces). The spin dependence at various fixed eccentricities is illustrated in the right three plots where the typical *V* profile is obvious irrespective of eccentricity.

maximally spinning black hole ($e = 0$, $a = 1$), the behavior of $z_-^2$ as a function of $p$ is described by

$$z_1^2 = -\frac{p^2(-3\sqrt{p} + 2\sqrt{3p + 2\sqrt{p} + 3} - 3)}{3\sqrt{p} - 1}. \quad \text{(A6)}$$

Furthermore when $e = 1$, $a = 1$,

$$z_1^2 = \frac{8\sqrt{2}p^{7/2} - 3p^4 - 4p^3 + 4p^2}{4(9p^2 + 4p + 4)}. \quad \text{(A7)}$$

On the equatorial plane $z_- = 0$ and $r_4 = 0$. Just as for the resonances the strongest spin dependent effects can be observed here. The behavior of the ISO can be well characterized by merely examining the behavior on the equator. As inclination increases, the location on the ISO will lie between the extremes of the prograde and retrograde values found on the equatorial plane. The characteristic $V$-$I$ transition seen in the resonances occurs for the ISO as well. If $r_4 = 0$ only the constant term (with respect to $r_4$) in Eq. (12) with Eq. (A2) substituted remains. This term results in a quartic equation for $p$ that implicitly defines the location of the ISO on the equator, as also found in [82],

$$(p - 6 - 2e)^2 p^2 + a^4(1 + e)^2(3 - e)^2 - 2a^2(1 + e)p[2(e^2 + 7) + (3 - e)p] = 0. \quad \text{(A8)}$$

If the black hole is nonspinning, $a = 0$, then $p = 6 + 2e$. If it is maximally spinning, $a = 1$, there are three roots to Eq. (A8), namely $p = 5 + e \pm 4\sqrt{1 + e}$ and a double root at $p = 1 + e$. Of these the correct limiting cases for the retro- and prograde ISO orbits are $p_- = 5 + e + 4\sqrt{1 + e}$ and $p_+ = 1 + e$ respectively. Thus the maximum splitting between the pro- and retrograde branches on the equatorial plane is $p_- - p_+ = 4(1 + \sqrt{1 + e})$.

If $a \neq 0$ the ISO can be found by solving the quartic. [For plotting purposes it is easier to consider Eq. (A8) to be a quadratic equation for $a^2$ and plot the square root of the result as a function of $p$.] For convenience, the leading-order spin dependence is also given here,

$$p_\mp = 6 + 2e \pm 4a\sqrt{2\left(\frac{1 + e}{3 + e}\right)} + O(a^2). \quad \text{(A9)}$$

## APPENDIX B: PROPERTIES OF CARLSON'S INTEGRALS

Carlson [35] [33] [34] has provided us with a number of symmetric, rapidly convergent schemes to evaluate elliptic integrals both numerically and analytically. This appendix summarizes the identities and properties associated with Carlson's integrals used in the body of the paper. Carlson showed that any elliptic integrals of the form

$$I_1 = \int_y^x \frac{dt}{\sqrt{(\alpha_1 + \beta_1 t)(\alpha_2 + \beta_2 t)(\alpha_3 + \beta_3 t)(\alpha_4 + \beta_4 t)}} \quad \text{(B1)}$$

can be expressed as

$$I_1 = 2R_F(U_{12}^2, U_{13}^2, U_{14}^2), \quad \text{(B2)}$$

where

$$U_{ij} = (X_i X_j Y_k Y_m + Y_i Y_j X_k X_m)/(x - y), \quad X_i = (\alpha_i + \beta_i x)^{1/2}, \quad Y_i = (\alpha_i + \beta_i y)^{1/2} \quad \text{(B3)}$$

and

$$R_F(\alpha, \beta, \gamma) = \frac{1}{2}\int_0^\infty \frac{dt}{\sqrt{(t + \alpha)(t + \beta)(t + \gamma)}}. \quad \text{(B4)}$$

This symmetric representation greatly reduces the number of parameters from ten in Eq. (B1) to the three arguments in Eq. (B4). All integrals have the same boundary conditions and the arguments enter only in the denominator of the integrand. An added advantage of using Carlson's integrals is that they obey a number of identities that make manipulation of the parameters that enter as arguments possible without necessarily evaluating the integral. These identities include the duplication theorem,

$$R_F(\alpha, \beta, \gamma) = 2R_F(\alpha + \lambda, \beta + \lambda, \gamma + \lambda), \quad \text{(B5)}$$

where $\lambda = (\alpha\beta)^{1/2} + (\alpha\gamma)^{1/2} + (\beta\gamma)^{1/2}$; and the fact that Carlson's function is homogeneous of degree $-\frac{1}{2}$,

$$R_F(\lambda\alpha, \lambda\beta, \lambda\gamma) = \lambda^{-1/2} R_F(\alpha, \beta, \gamma), \quad \text{(B6)}$$

for any $\lambda$ and a number of special symmetric cases that can easily be evaluated,

$$R_F(\beta, \beta, \beta) = \beta^{-1/2}, \quad R_F(0, \beta, \beta) = \frac{\pi}{2}\beta^{-1/2}. \quad \text{(B7)}$$

If the first argument is $\alpha = 0$ a restricted version of the duplication theorem also holds: for $x > 0$, $y > 0$, $z = (x + y)/2$,

$$R_F(0, x^2, y^2) = R_F(0, xy, z^2). \quad \text{(B8)}$$

For small deviations from the symmetric case it is possible to construct a rapidly converging series. We now derive this series for $R_F(0, y + \delta, y - \delta)$. Start with the integral representation of $R_F$, Eq. (B4) in the special case,

$$R_F(0, y + \delta, y - \delta) = \frac{1}{2}\int_0^\infty \frac{dt}{\sqrt{t(t + y + \delta)(t + y - \delta)}}, \quad \text{(B9)}$$

and make a Taylor series expansion of the integrand in terms of $\delta$. Integrate the result term by term to yield

$$R_F(0, y+\delta, y-\delta) = \frac{\pi}{2\sqrt{y}}\left(1 + \frac{3\delta^2}{16y^2} + \frac{105\delta^4}{1024y^4}\right) + \frac{\pi}{2\sqrt{y}}\left(\frac{1155\delta^6}{16384y^6} + \frac{225225\delta^8}{4194304y^8} + O(\delta^{10})\right). \quad \text{(B10)}$$

Since only quadratic terms in the parameter $\delta/y$ appear this series converges very rapidly. To complete the discussion on Carlson's integrals and mainly for comparison with other work we now give the relationship between Carlson's integrals and some of the elliptic functions,

$$R_f(0, 1-k^2, 1) = K(k), \quad \text{(B11)}$$

$$R_F(0, \alpha, \beta) = \beta^{-1/2} K(\sqrt{1-\alpha/\beta}). \quad \text{(B12)}$$

Here $K(k)$ is the complete elliptic integral of the first kind.


[1] R. Giffen, Astron. Astrophys. **23**, 387 (1973).
[2] J. Hänninen, *Granular gases*, Lecture Notes in Physics Vol. 564 (Springer, Berlin, Heidelberg, 2001), p. 350–362.
[3] S. F. Dermott and C. D. Murray, Nature (London) **290**, 664 (1981).
[4] P. Goldreich and S. Tremaine, Annu. Rev. Astron. Astrophys. **20**, 249 (1982).
[5] N. Murray and M. Holman, Nature (London) **410**, 773 (2001).
[6] S. Doeleman, in *10th European VLBI Network Symposium and EVN Users Meeting: VLBI and the New Generation of Radio Arrays*, http://pos.sissa.it/cgi-bin/reader/conf.cgi?confid=125.
[7] J. Brink, M. Geyer, and T. Hinderer, Phys. Rev. Lett. **114**, 081102 (2015).
[8] R. Grossman, J. Levin, and G. Perez-Giz, Phys. Rev. D **85**, 023012 (2012).
[9] U. Ruangsri and S. A. Hughes, Phys. Rev. D **89**, 084036 (2014).
[10] R. Grossman, J. Levin, and G. Perez-Giz, Phys. Rev. D **88**, 023002 (2013).
[11] R. Grossman, J. Levin, and G. Perez-Giz, Phys. Rev. D **85**, 023012 (2012).
[12] C. M. Hirata, Mon. Not. R. Astron. Soc. **414**, 3212 (2011).
[13] G. Contopoulos, G. Lukes-Gerakopoulos, and T. A. Apostolatos, Int. J. Bifurcation Chaos Appl. Sci. Eng. **21**, 2261 (2011).
[14] G. Contopoulos, M. Harsoula, and G. Lukes-Gerakopoulos, Celestial Mechanics and Dynamical Astronomy **113**, 255 (2012).
[15] J. R. Gair, C. Li, and I. Mandel, Phys. Rev. D **77**, 024035 (2008).
[16] J. Brink, Phys. Rev. D **78**, 102002 (2008).
[17] M. Geyer, MSc thesis, Stellenbosch University, 2013, http://scholar.sun.ac.za.
[18] O. Semerk and P. Sukov, Mon. Not. R. Astron. Soc. **425**, 2455 (2012).
[19] M. D. Hartl, Phys. Rev. D **67**, 024005 (2003).
[20] M. D. Hartl, Phys. Rev. D **67**, 104023 (2003).
[21] S. Suzuki and K.-I. Maeda, Phys. Rev. D **55**, 4848 (1997).
[22] É. É. Flanagan and T. Hinderer, Phys. Rev. Lett. **109**, 071102 (2012).
[23] E. E. Flanagan, S. A. Hughes, and U. Ruangsri, arXiv:1208.3906.
[24] M. van de Meent, Phys. Rev. D **89**, 084033 (2014).
[25] C. Hirata, Phys. Rev. D **83**, 104024 (2011).
[26] M. van de Meent, Phys. Rev. D **90**, 044027 (2014).
[27] N. Warburton, L. Barack, and N. Sago, Phys. Rev. D **87**, 084012 (2013).
[28] W. Schmidt, Classical Quantum Gravity **19**, 2743 (2002).
[29] T. Hinderer and E. E. Flanagan, Phys. Rev. D **78**, 064028 (2008).
[30] G. Török, M. A. Abramowicz, W. Kluźniak, and Z. Stuchlik, Astron. Astrophys. **436**, 1 (2005).
[31] J. D. Schnittman and E. Bertschinger, Astrophys. J. **606**, 1098 (2004).
[32] R. Fujita and W. Hikida, Classical Quantum Gravity **26**, 135002 (2009).
[33] DLMF, NIST Digital Library of Mathematical Functions, http://dlmf.nist.gov/, Release 1.0.5 of 2012-10-01.
[34] *NIST Handbook of Mathematical Functions*, edited by F. W. J. Olver, D. W. Lozier, R. F. Boisvert, and C. W. Clark (Cambridge University Press, New York, NY, 2010).
[35] B. Carlson, Numerical Algorithms **10**, 13 (1995).
[36] B. Carter, Phys. Rev. **174**, 1559 (1968).
[37] E. Barausse and L. Rezzolla, Phys. Rev. D **77**, 104027 (2008).
[38] D. Psaltis, Astrophys. J. **759**, 130 (2012).
[39] B. Kocsis, N. Yunes, and A. Loeb, Phys. Rev. D **84**, 024032 (2011).
[40] N. Yunes, M. C. Miller, and J. Thornburg, Phys. Rev. D **83**, 044030 (2011).
[41] P. Gondolo and J. Silk, Phys. Rev. Lett. **83**, 1719 (1999).
[42] L. Sadeghian, F. Ferrer, and C. Will, Phys. Rev. D **88**, 063522 (2013).
[43] N. A. Collins and S. A. Hughes, Phys. Rev. D **69**, 124022 (2004).
[44] S. J. Vigeland and S. A. Hughes, Phys. Rev. D **81**, 024030 (2010).

[45] T. Johannsen and D. Psaltis, Phys. Rev. D **83**, 124015 (2011).
[46] L. Barack and C. Cutler, Phys. Rev. D **75**, 042003 (2007).
[47] K. Glampedakis and S. Babak, Classical Quantum Gravity **23**, 4167 (2006).
[48] J. Gair and N. Yunes, Phys. Rev. D **84**, 064016 (2011).
[49] N. Cornish, L. Sampson, N. Yunes, and F. Pretorius, Phys. Rev. D **84**, 062003 (2011).
[50] L. Barack, Classical Quantum Gravity **26**, 213001 (2009).
[51] J. Steinhoff and D. Puetzfeld, Phys. Rev. D **86**, 044033 (2012).
[52] V. I. Arnold, Russ. Math. Surv. **18**, 9 (1963).
[53] J. Moser, *Stable and Random Motions in Dynamical Systems* (Princeton University Press, Princeton, NJ, 1973).
[54] H. G. Schuster and W. Just, *Deterministic Chaos, An Introduction* (Wiley-VCH Verlag GmbH & Co. KGaA, Weinheim, 2005).
[55] A. J. Lichtenberg and M. Lieberman, *Regular and Chaotic Dynamics*, 2nd ed. (Springer-Verlag, Berlin, 1992).
[56] C. A. Perez, A. S. Silbergleit, R. V. Wagoner, and D. E. Lehr, Astrophys. J. **476**, 589 (1997).
[57] M. A. Abramowicz and P. C. Fragile, Living Rev. Relativity **16**, 1 (2013).
[58] K. Glampedakis and S. Babak, Classical Quantum Gravity **23**, 4167 (2006).
[59] G. Contopoulos, *Order and Chaos in Dynamical Astronomy* (Springer, Berlin, Heildelberg, New York, 2002).
[60] N. Voglis and C. Efthymiopoulos, J. Phys. A **31**, 2913 (1998).
[61] V. I. Arnol'D, V. V. Kozlov, A. I. Neishtadt, A. I. Nejshtadt, and A. Iacob, *Mathematical Aspects of Classical and Celestial Mechanics* (Springer-Verlag, Berlin, 2006), p. 1.
[62] B. V. Chirikov, Phys. Rep. **52**, 263 (1979).
[63] J. Brink and T. Hinderer (to be published).
[64] D. F. Escande and F. Doveil, J. Stat. Phys. **26**, 257 (1981).
[65] C. Chandre and H. R. Jauslin, Phys. Rep. **365**, 1 (2002).
[66] K. Whiteman, Rep. Prog. Phys. **40**, 1033 (1977).
[67] C. Chicone, B. Mashhoon, and D. G. Retzloff, J. Phys. A **33**, 513 (2000).
[68] C. Robinson, Lect. Notes Math. **1007**, 651 (1983).
[69] S. S. Doeleman *et al.*, Nature (London) **455**, 78 (2008).
[70] V. L. *et al.*, Astrophys. J. **727**, L36 (2011).
[71] R. A. Remillard and J. E. McClintock, Annu. Rev. Astron. Astrophys. **44**, 49 (2006).
[72] M. Gierliński, M. Middleton, M. Ward, and C. Done, Nature (London) **455**, 369 (2008).
[73] R. C. Reis, J. M. Miller, M. T. Reynolds, K. Gültekin, D. Maitra, A. L. King, and T. E. Strohmayer, Science **337**, 949 (2012).
[74] M. A. Abramowicz and W. Kluźniak, Astrophys. J. **374**, L19 (2001).
[75] R. V. Wagoner, A. S. Silbergleit, and M. Ortega-Rodríguez, Astrophys. J. Lett. **559**, L25 (2001).
[76] T. Johannsen and D. Psaltis, Astrophys. J. **726**, 11 (2011).
[77] L. Rezzolla, S. Yoshida, T. J. Maccarone, and O. Zanotti, Mon. Not. R. Astron. Soc. **344**, L37 (2003).
[78] D. Lai and D. Tsang, Mon. Not. R. Astron. Soc. **393**, 979 (2009).
[79] K. Liu, N. Wex, M. Kramer, J. M. Cordes, and T. J. W. Lazio, Astrophys. J. **747**, 1 (2012).
[80] L. Sadeghian and C. M. Will, Classical Quantum Gravity **28**, 225029 (2011).
[81] S. Gillessen, F. Eisenhauer, S. Trippe, T. Alexander, R. Genzel, F. Martins, and T. Ott, Astrophys. J. **692**, 1075 (2009).
[82] R. O'Shaughnessy, Phys. Rev. D **67**, 044004 (2003).